Electronic Supplementary Material (ESI) for ChemComm.

SUPPORTING INFORMATION FOR

Unexpected Reactivity of a PONNOP 'Expanded Pincer' Ligand

Arthur R. Scheerder,[a] Martin Lutz,[b] Daniël L. J. Broere*[a]

a Organic Chemistry & Catalysis, Debye Institute for Nanomaterials Science, Utrecht University, Universiteitsweg 99, 3584 CG Utrecht, The Netherlands

b Crystal and Structural Chemistry, Bijvoet Centre for Biomolecular Research, Faculty of Science, Utrecht University, Padualaan 8, 3584 CH Utrecht, The Netherlands

NMR data files and ORCA input and output files can be obtained free of charge from:
http://doi.org/10.4121/uuid:8fd78884-01b0-4c37-a4ca-fb1cf4af8b61

Index

Materials and methods

General considerations All manipulations were performed under inert atmosphere using standard Schlenk techniques or inside of a N_2-filled M. Braun glovebox using dry solvents and reagents, unless stated otherwise. Glassware was dried at 130 °C, unless noted otherwise. Solvents were collected from an M. Braun MB-SPS-800 solvent purification system and stored over 4 Å molecular sieves, apart from pentane (which was only degassed and stored over 4 Å molecular sieves) and CH_2Cl_2 (which was stored over 3 Å molecular sieves). Deuterated solvents were obtained from Cambridge Isotope Laboratories (except THF-d_8, which was obtained from ABCR), degassed and stored over 4 Å molecular sieves. All commercial reagents were used as received and were obtained from Sigma Aldrich or Acros. NMR data was recorded on an Agilent MRF 400 equipped with a OneNMR probe and Optima Tune system or a Varian VNMR-S-400 equipped with a PFG probe. All resonances in ^{1}H-NMR were referenced to residual solvent peaks (7.16 for C_6D_6, 5.32 for CD_2Cl_2), apart from ^{1}H NMR spectra obtained in non-deuterated solvents where the solvent peak was used (1.73 for THF). The assignment of peaks is based on relative integration, chemical shift, and 2D NMR analysis (COSY and HSQC). IR-data was recorded on a PerkinElmer SpectrumTwo Infrared Spectrophotometer equipped with an ATR-probe. Elemental analysis was performed by MEDAC Ltd. based in the United Kingdom.

Synthesis and characterization

2,7-dihydroxy-1,8-naphthyridine

All manipulations in this procedure were performed under aerobic conditions using technical grade solvents and non-dried glassware. The synthesis was performed according to a modified literature procedure.[1]

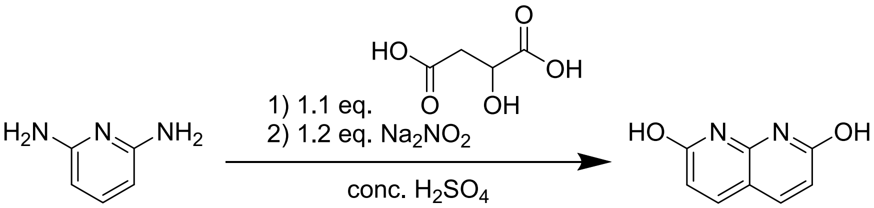

Solid 2,6-diaminopyridine (8.73 g, 80.0 mmol) was added slowly to vigorously stirred conc. H_2SO_4 (80 mL) in a 500 mL round-bottom flask. The resulting brown solution was cooled in an ice bath for 10 minutes after which finely ground L-malic acid (11.80 g, 88.0 mmol) was added under continued cooling. The ice bath was removed, a gas trap was connected to the reaction flask and the mixture was heated at 110 °C until no more gas evolution was observed (approx. 1 h). The mixture was cooled in an ice bath and $NaNO_2$ (6.62 g; 96.0 mmol) was slowly added over the course of 5 min. After stirring the dark red mixture for 10 min the ice bath was removed. After stirring for 30 min at ambient temperature the mixture was poured into a 5 L beaker containing ice (630 g) upon which heat and gas evolution was observed. After the ice had melted a 4 M aqueous K_2CO_3 solution (0.4 L) was carefully added to the mixture. Subsequently, the mixture was acidified by slow addition of acetic acid (25 mL) after which the solids were filtered off using a glass frit (NOTE: Use a large filter as the solids tends to clog up the filter). The residue was suspended in EtOH (250 mL) and stirred vigorously for 5 minutes. The mixture was cooled and the solids were filtered off. The obtained solid was subsequently suspended in water (1.0 L), stirred vigorously, filtered off and washed with additional water (approx. 50 mL). The residue was washed with EtOH (100 mL), and Et_2O (100 mL) and dried under a dynamic vacuum to give a yellow solid (7.96 g, 45%, 74% purity by weight*).

^{1}H NMR (400 MHz, DMSO-d$_6$ 298K): δ = 11.78 (s, 2H), 7.80 (d, $^3J_{H,H}$ = 9.0 Hz, 2H), 6.32 (d, $^3J_{H,H}$ = 9.0 Hz, 2H).

* The ^{1}H NMR spectrum of the obtained material (Fig. S1) is in agreement with the previously reported spectrum.**Error! Bookmark not defined.** Similar to the material obtained when following the literature procedure, we found that the obtained product contained an NMR silent impurity. This is likely an inorganic potassium salt that is formed in the reaction and was found not to affect subsequent reactions. However, to be able to proper balance reaction stoichiometry a spectroscopic purity (74 wt%) was determined by ^{1}H NMR analysis (Fig. S1) using 1,4-dimethoxybenzene as an internal standard.

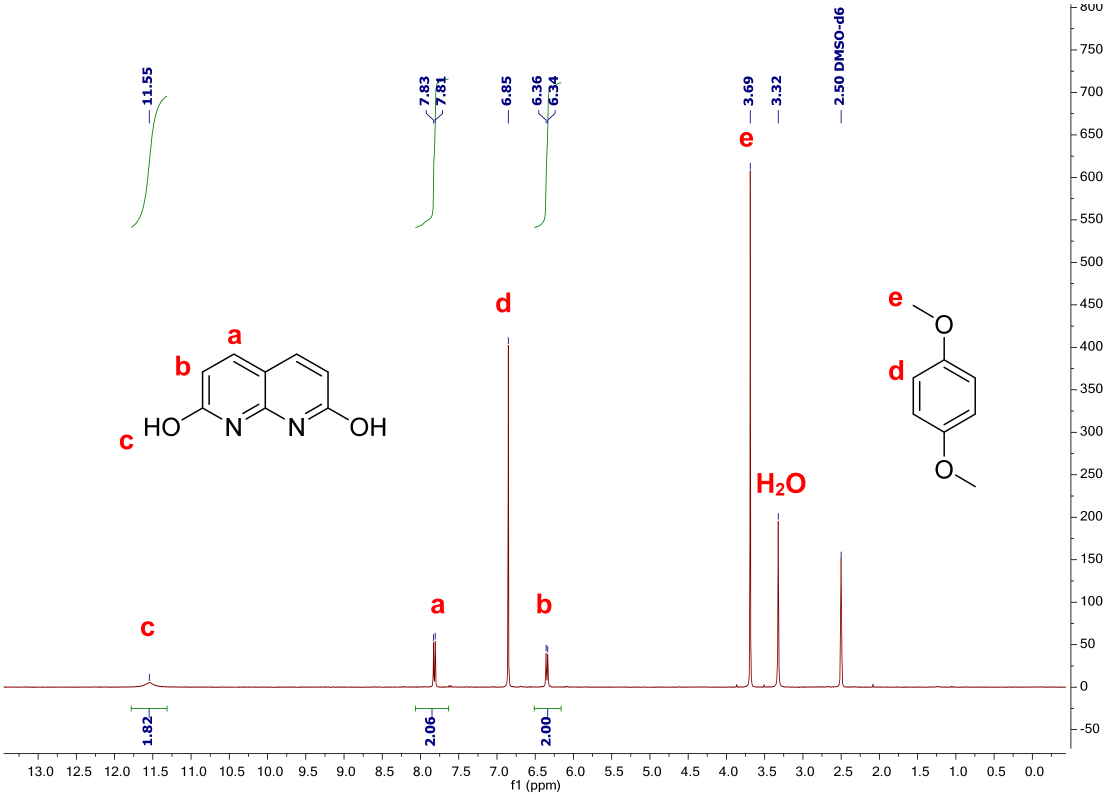

Figure S1. The ^{1}H NMR spectrum of a mixture of 2,7-dihydroxy-1,8-naphthyridine and the internal standard 1,4-dimethoxybenzene in DMSO-d$_6$ at 25 °C to determine the purity.

Synthesis of $^{i\text{-}Pr}$PONNOP

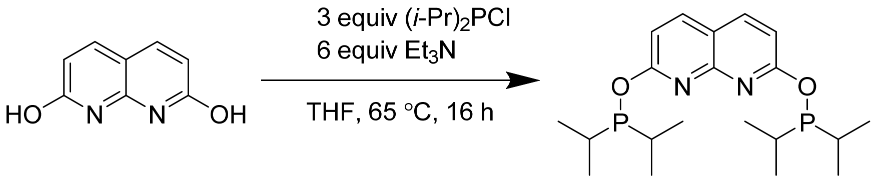

A Schlenk flask was charged with 2,7-dihydroxy-1,8-naphthyridine (2.22 g, 74% pure, 10.1 mmol), THF (40 mL) and NEt_3 (8.40 mL, 60.3 mmol). Chlorodiisopropylphosphine (3.50 mL, 21.8 mmol) was added dropwise to the Schlenk and the mixture was heated at 65 °C for 16 h. Subsequently, additional chlorodiisopropylphosphine (0.80 mL, 5.0 mmol) was added and the mixture was heated at 65 °C for an additional 30 minutes. After cooling to ambient temperature, the brown reaction mixture was filtered and the residue was extracted with THF (10 mL). The combined organic fractions were concentrated under a dynamic vacuum to give a brown oil. The residue was extracted with *n*-hexane (20 mL), the extracts were filtered and concentrated under a dynamic vacuum. The residue was dried under a dynamic vacuum for 16 h to give a brown oil (3.64 g, 82%, 90% purity*).

* The reactions conditions were based on the literature procedure for the $^{i\text{-}Pr}$PONOP pincer ligand[2] , which also was obtained in 90% purity. An alternative procedure[3] involving distillation of the $^{i\text{-}Pr}$PONOP was prohibited by the high molecular weight of **$^{i\text{-}Pr}$PONNOP**. Attempts to further increase the purity by extractions with various solvents, chromatography with silica or alumina and attempted crystallizations solely resulted in a decrease in purity. Hence, it is key to use rigorously dried solvents and reagents free of (organic) impurities in the synthesis of, and in reactions with **$^{i\text{-}Pr}$PONNOP**.

^{1}H NMR (400 MHz, C_6D_6 298K): δ = 7.19 (d, $^3J_{H,H}$ = 8.6 Hz, 2H), 6.66 (d, $^3J_{H,H}$ = 8.6 Hz, 2H), 1.99 (pd, $^2J_{P,H}$ = 2.1 Hz, $^3J_{H,H}$ = 7.2 Hz, 4H), 1.21 (m, 24H).

^{31}P{^{1}H} NMR (162 MHz, C_6D_6, 298K): δ = 148.2 (s).

^{13}C{^{1}H} NMR (101 MHz, C_6D_6, 298 K): δ = 165.4 (s, 1C), 165.3 (s, 1C), 138.8 (s, 2C), 116.1 (s, 1C), 111.5 (s, 2C), 28.3 (d, 4C), 18,1 (m, 8C).

ATR-IR: ν [cm^{-1}] = 2952, 2926, 2866, 1661, 1602, 1496, 1463, 1429, 1398, 1383, 1323, 1312, 1258, 1232, 1125, 867, 840, 796, 661, 614.

Anal. Calcd. For $C_{20}H_{32}N_2O_2P_2$: C 60.90, H 8.18, N 7.10. Found: C 60.81, H 8.01, N 6.82.

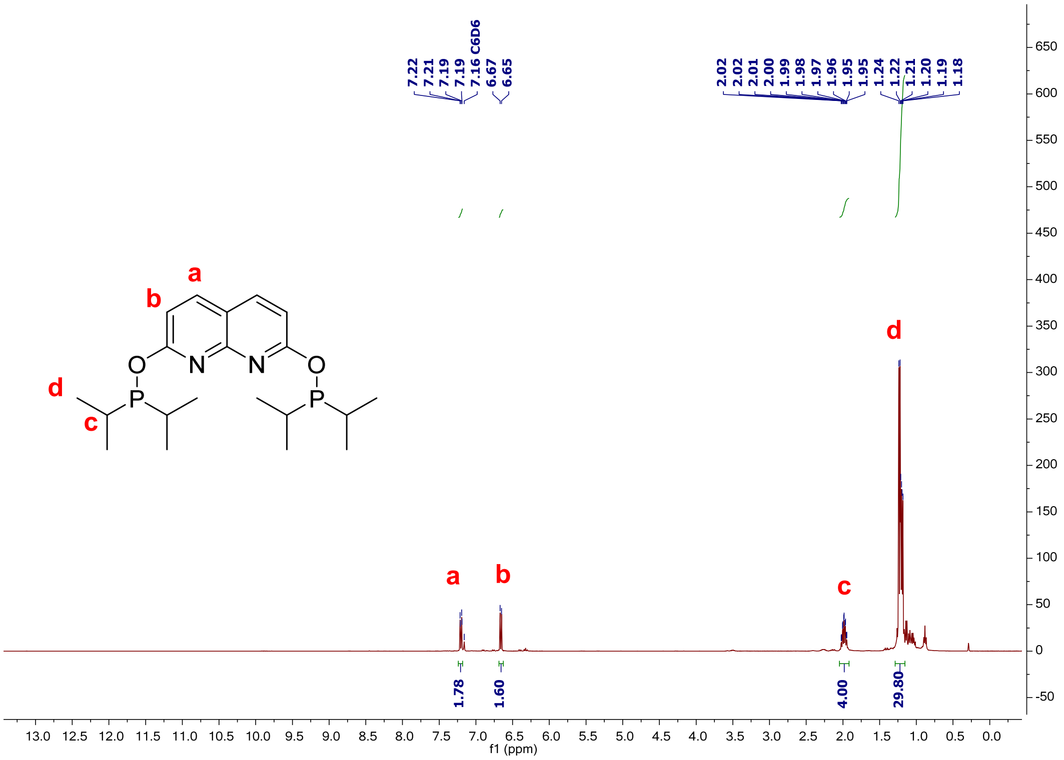

Figure S2: The ^{1}H NMR spectrum of $^{i\text{-Pr}}$PONNOP in C_6D_6 at 25 °C.

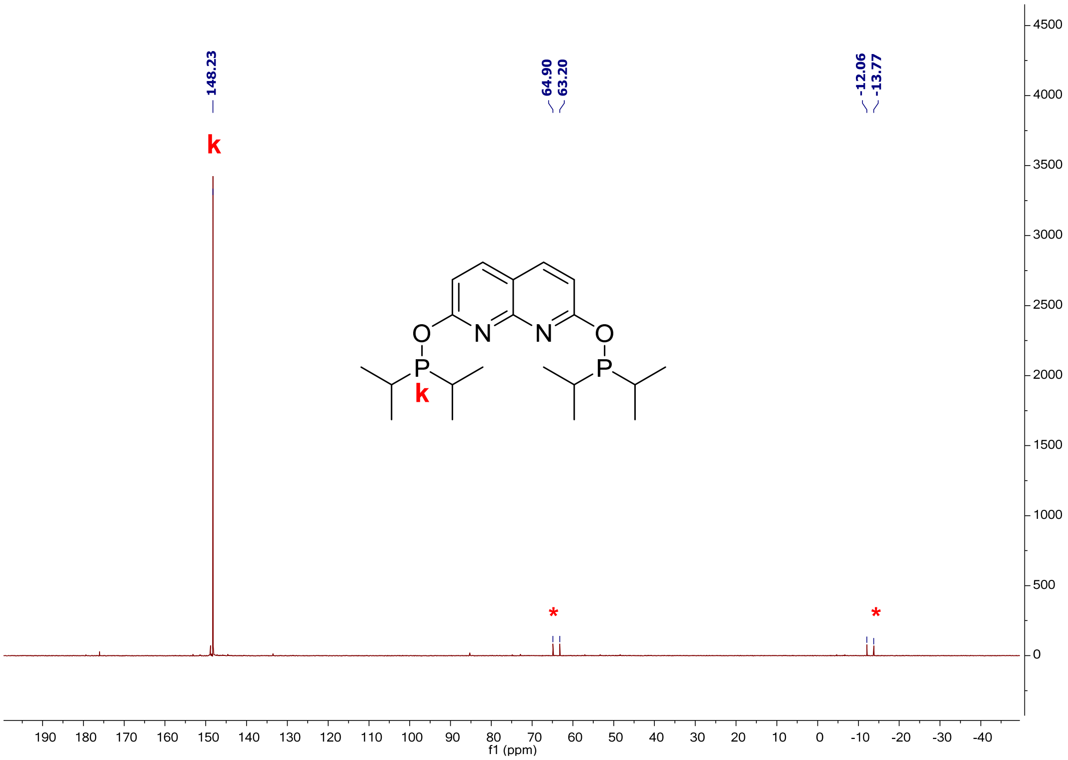

Figure S3: The ^{31}P NMR spectrum of $^{i\text{-Pr}}$PONNOP in C_6D_6 at 25 °C. The resonances labelled with * are from an unidentified impurity.

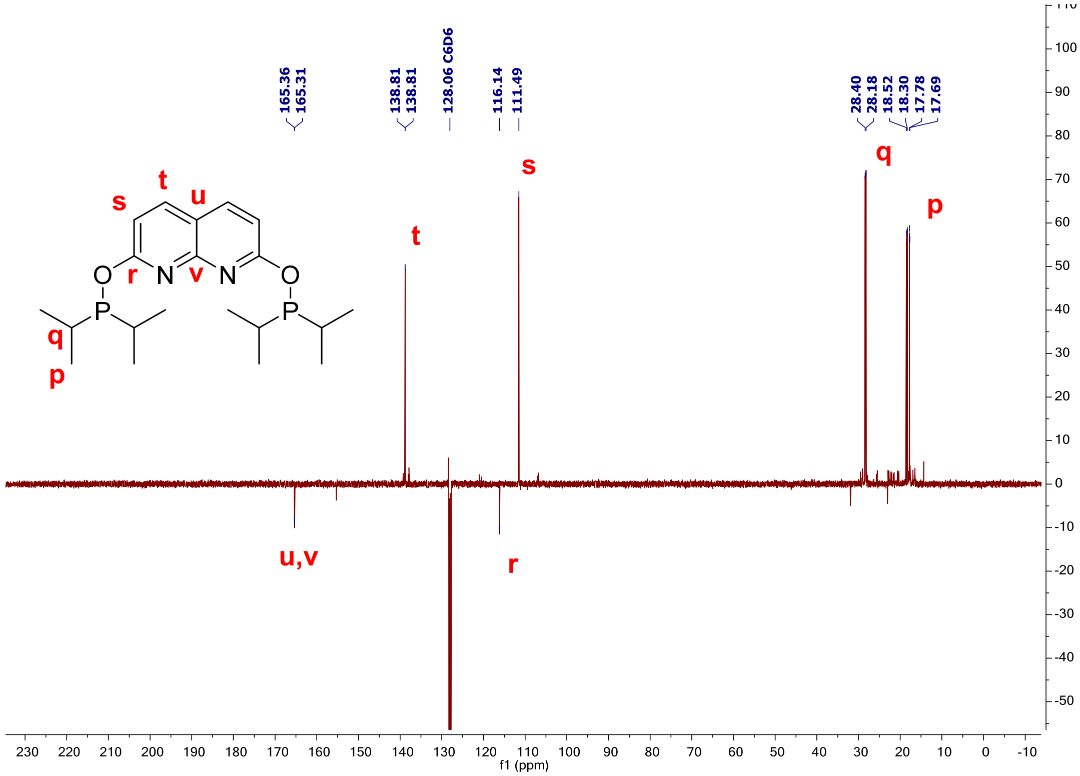

Figure S4: The ^{13}C (APT) NMR spectrum of $^{i\text{-Pr}}$PONNOP in C_6D_6 at 25 °C.

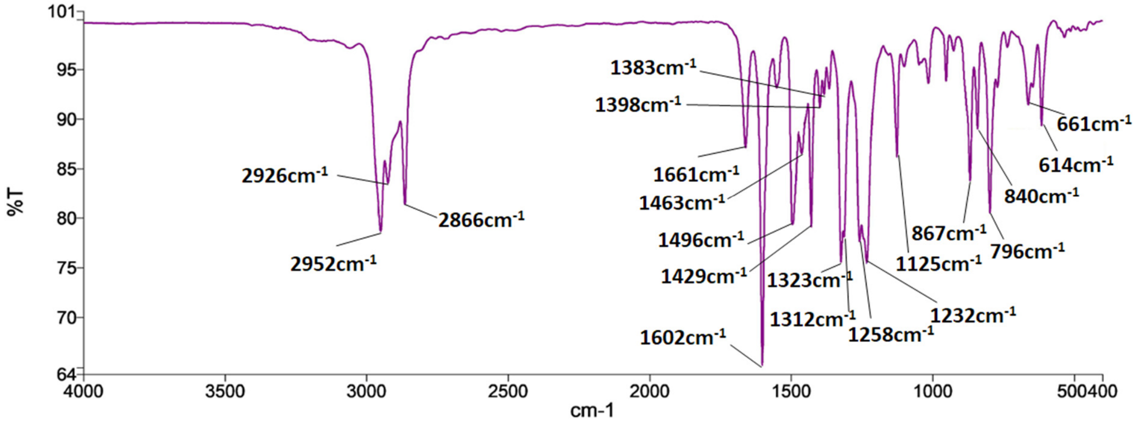

Figure S5: The IR-spectrum of $^{i\text{-Pr}}$PONNOP.

Synthesis of complex 1

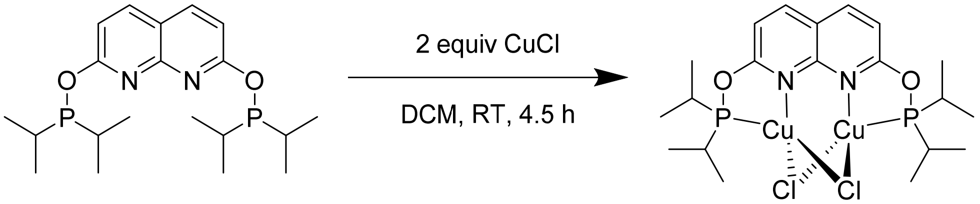

A solution of $^{i\text{-Pr}}$**PONNOP** (71.6 mg, 0.18 mmol) in CH_2Cl_2 (2.5 mL) was added to a vial containing CuCl (39.4 mg, 0.36 mmol). The orange-red suspension was stirred vigorously for 4.5 hours after which the suspension was filtered. The residue was washed with CH_2Cl_2 (0.5 mL) and the combined organic fractions were concentrated under a dynamic vacuum. The residue was ground into a fine orange powder washed with *n*-hexane (2 x 2.5 mL) and dried under a dynamic vacuum to give a pale orange solid (83.0 mg, 77%).

^{1}H NMR (400 MHz, C_6D_6, 298 K): δ = 7.03 (d, $^3J_{H,H}$ = 8.6 Hz, 2H), 6.40 (d, $^3J_{H,H}$ = 8.6 Hz, 2H), 1.86 (pd, $^3J_{H,H}$ = 7.1 Hz,$^2J_{H,P}$ = 2.1 Hz, 4H), 1.14 (d, $^3J_{H,H}$ = 6.9 Hz, 6H), 1.10 (d, $^3J_{H,H}$ = 7.1 Hz, 12H), 1.05 (d, $^3J_{H,H}$ = 7.2 Hz, 6H).

^{31}P{^{1}H} NMR (162 MHz, C_6D_6, 298 K): δ = 123.7 (s).

^{13}C{^{1}H} NMR (101 MHz, C_6D_6, 298 K): δ = 164.5 (s, 1C), 149.7 (s, 1C), 140.9 (s, 2C), 117.3 (s, 1C), 111.7 (s, 2C), 27.3 (d, 4C), 16.8 (m, 8C).

ATR-IR: ν [cm^{-1}] = 2958, 2929, 2868, 1599, 1556, 1500, 1484, 1464, 1428, 1325, 1261, 1237, 1216, 1130, 868, 852, 809, 796, 788, 685.

Anal. Calcd. For $C_{20}H_{32}N_2O_2P_2Cu_2Cl_2$: C 40.55, H 5.44, N 4.73. Found: C 40.20, H 5.74, N 4.51.*

** Although there are minor impurities (integration shows <5%) observed in the ^{1}H NMR spectrum of the obtained material, the combustion analysis data almost seems to agree too well. We reason that it is likely that the small amount of the impurity together with it having a similar chemical composition as the complex **1**, does not alter the found C H and N composition significantly from the expected values. Through recrystallization form hexane/THF mixtures we have obtained small amounts of Cu complex that does not feature this minor impurity in its ^{1}H NMR spectrum. Rather than cherry-picking pristine spectra, we aim for reproducibility in science and therefore feel very strongly that the presented NMR, IR, and combustion analysis should be representative of the material that is obtained when the described experimental procedure is followed to the letter.*

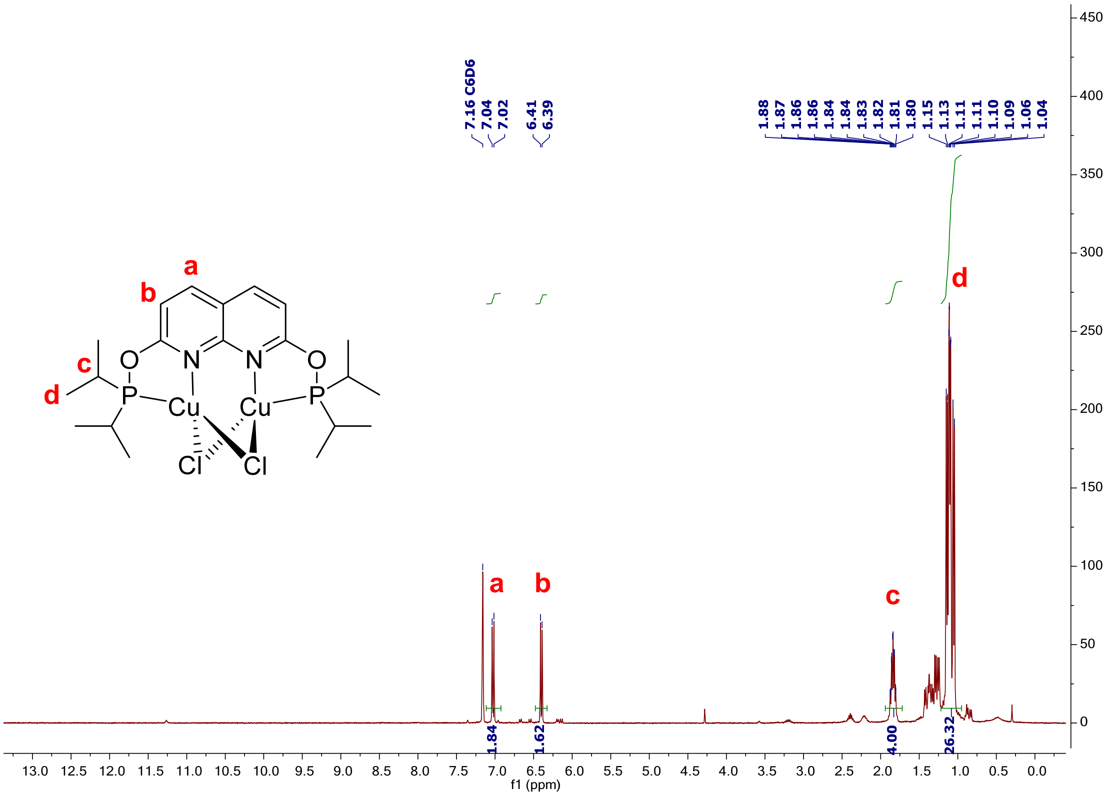

Figure S6: The ^{1}H NMR spectrum of **1** in C_6D_6 at 25 °C.

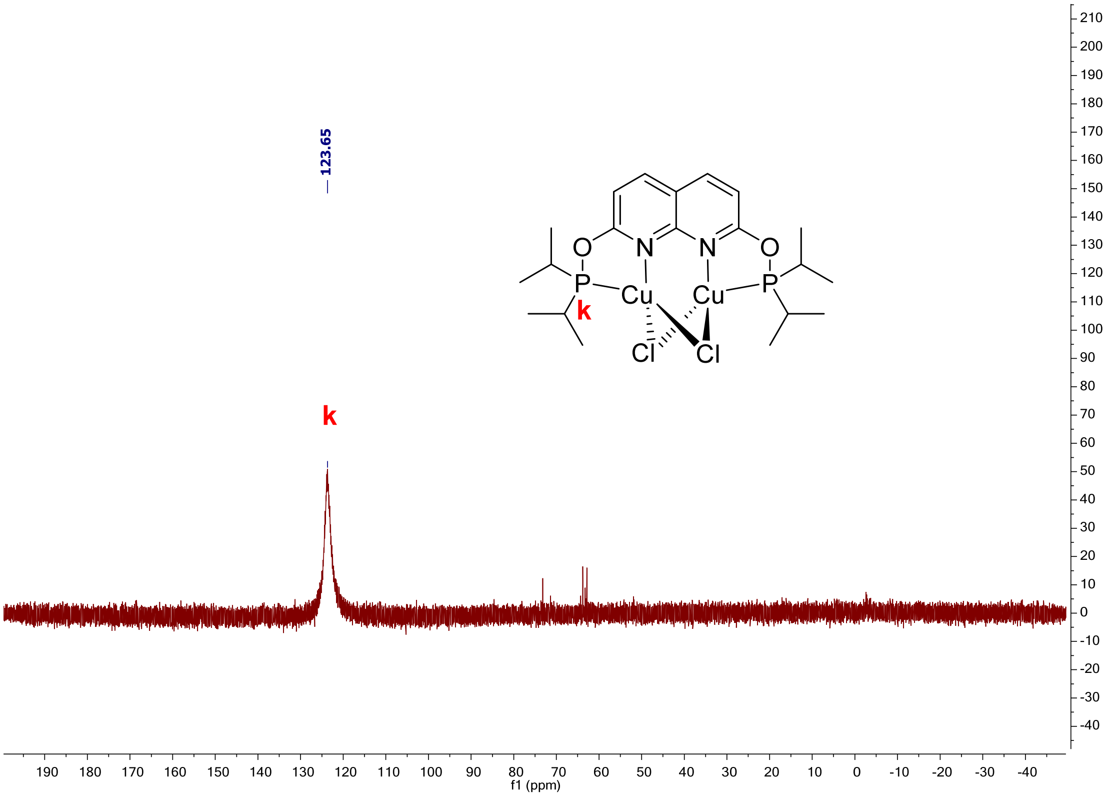

Figure S7: The ^{31}P NMR spectrum of **1** in C_6D_6 at 25 °C.

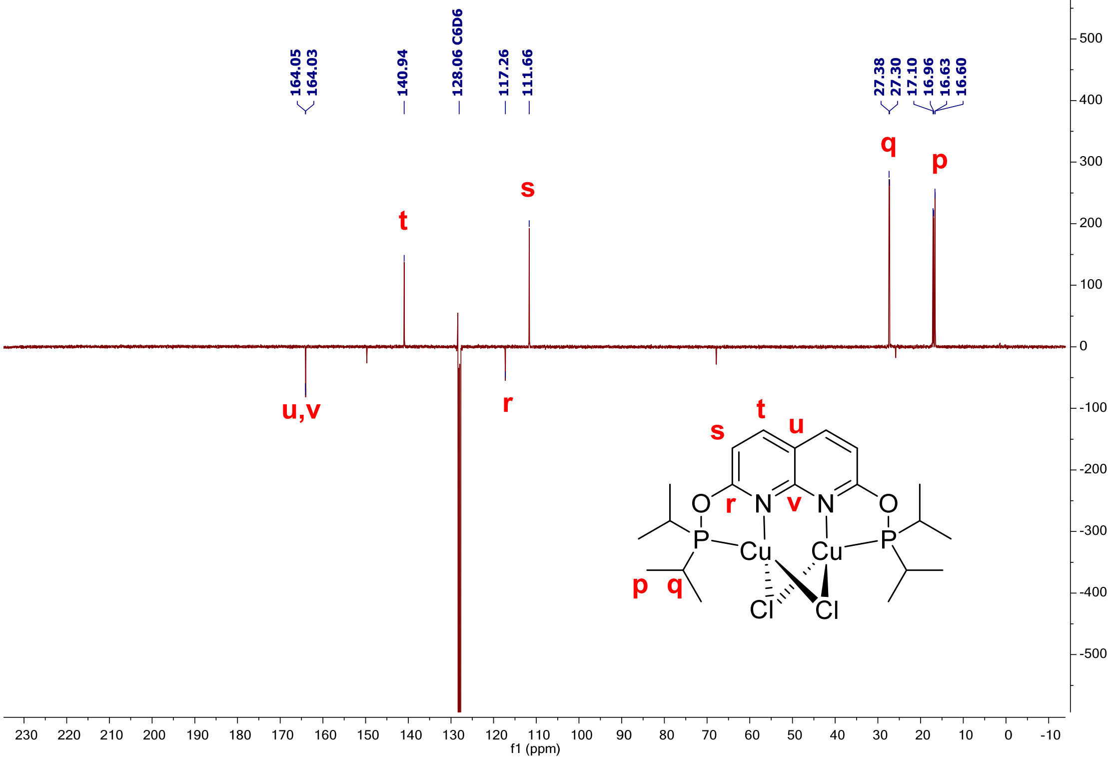

Figure S8: The ^{13}C (APT) NMR spectrum of **1** in C_6D_6 at 25 °C.

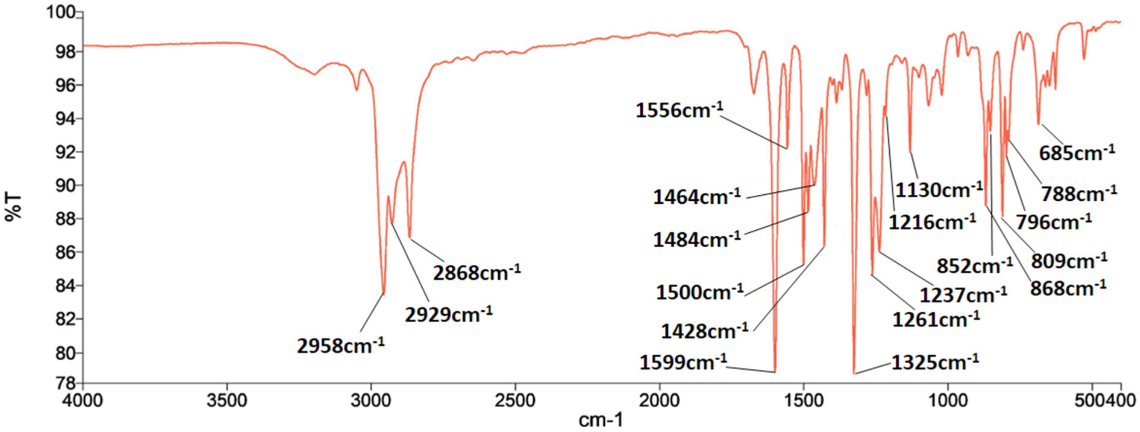

Figure S9: The IR-spectrum of **1**.

Synthesis of complex 2

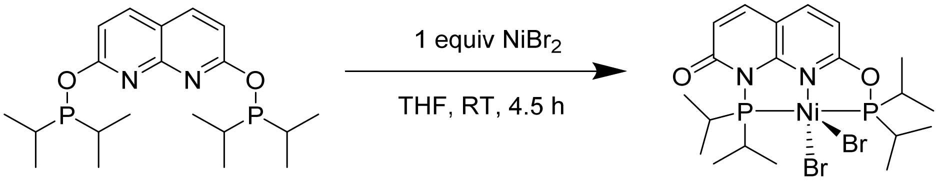

A solution of **$^{i\text{-Pr}}$PONNOP** (556 mg, 1.41 mmol) in THF (9.0 mL) was added dropwise to a vial containing $NiBr_2$ (307 mg, 1.40 mmol). The dark red suspension was stirred vigorously for 24 h after which all volatiles were removed under a dynamic vacuum. The residual dark red solid was extracted with CH_2Cl_2 (2 x 7 mL), the extracts were concentrated to approximately half the volume and *n*-pentane (10 mL) was added. The resulting mixture was placed at -40 °C for 2.5 hours after which a precipitate was filtered off and dried under a dynamic vacuum to give a red solid (739 mg). Further reduction of the mother liquor and placing it at -40 °C afforded a 2nd crop of the product (25.1 mg). Combined yield: 764 mg (89%).

^{1}H NMR (400 MHz, CD_2Cl_2, 298 K): 9.17 (s, 1H), 8.33 (d, $^3J_{H,H}$ = 9.5 Hz, 1H), 7.35 (d, $^3J_{H,H}$ = 6.5 Hz, 1H), 6.33 (d, $^3J_{H,H}$ = 9.4 Hz, 1H), 3.48 – 3.42 (m, 2H), 3.00 – 2.95 (m, 2H), 1.61 – 1.45 (m, 24H).

^{31}P{^{1}H} NMR (162 MHz, CD_2Cl_2, 298 K): δ = 192.0 (d, $^2J_{P,P}$ = 326 Hz), 131.5 (d, $^2J_{P,P}$ = 326 Hz).

^{13}C{^{1}H} NMR (101 MHz, CD_2Cl_2, 298 K): δ = 166.4 (s, 1C), 164.0 (s, 1C), 154.4 (s, 1C), 145.3 (s, 1C), 143.4 (s, 1C), 121.8 (s, 1C), 114.1 (s, 1C), 108.6 (s, 1C), 30.0 (s, 1C), 29.8 (s, 1C), 28.2 (s, 1C), 28.0 (s, 1C), 19.9 (s, 2C), 18.7 (s, 2C), 18.0 (s, 2C), 17.5 (s, 2C).

ATR-IR: ν [cm^{-1}] = 3047, 2967, 2932, 2872, 1679, 1643, 1626, 1585, 1560, 1462, 1409, 1392, 1368, 1343, 1224, 1130, 1065, 1028, 981, 887, 887, 847, 788, 776, 693, 672, 631, 531, 505, 478, 432.

Anal. Calcd. For $C_{20}H_{32}Br_2N_2NiO_2P_2$: C 39.19, H 5.26, N 4.57. Found C 39.08, H 5.30, N 4.51.

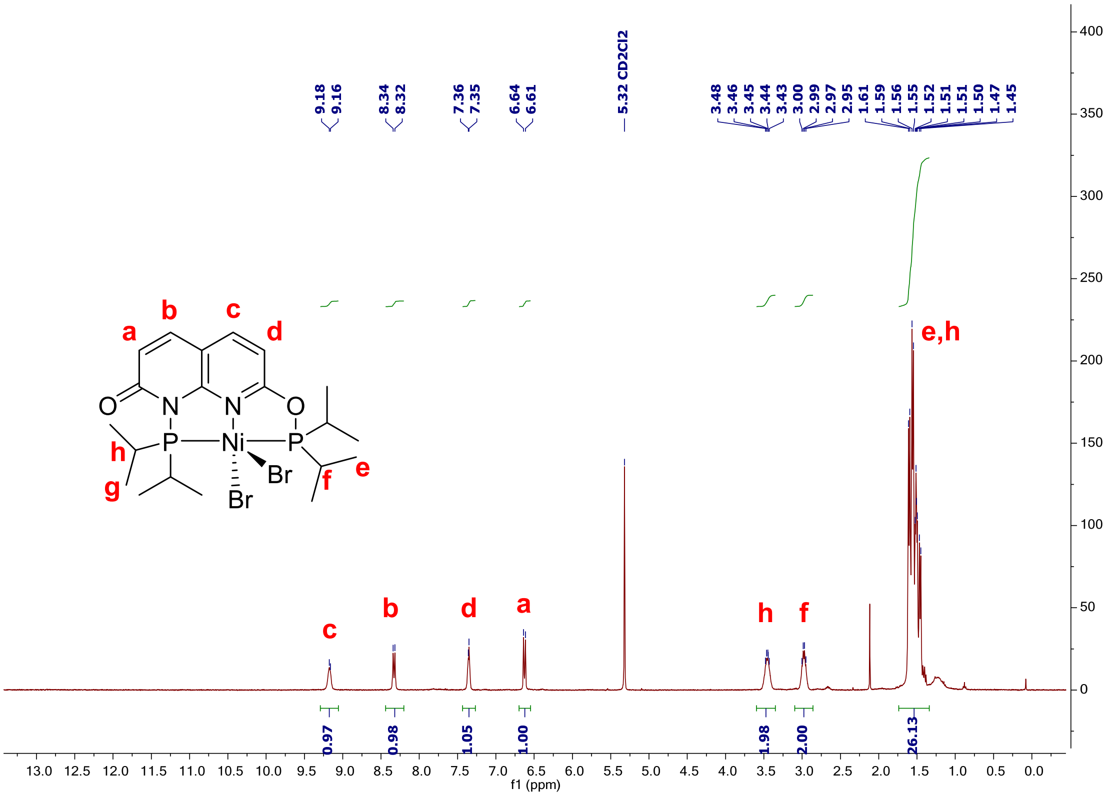

Figure S10: The ^{1}H NMR spectrum of **2** in CD_2Cl_2 at 25 °C.

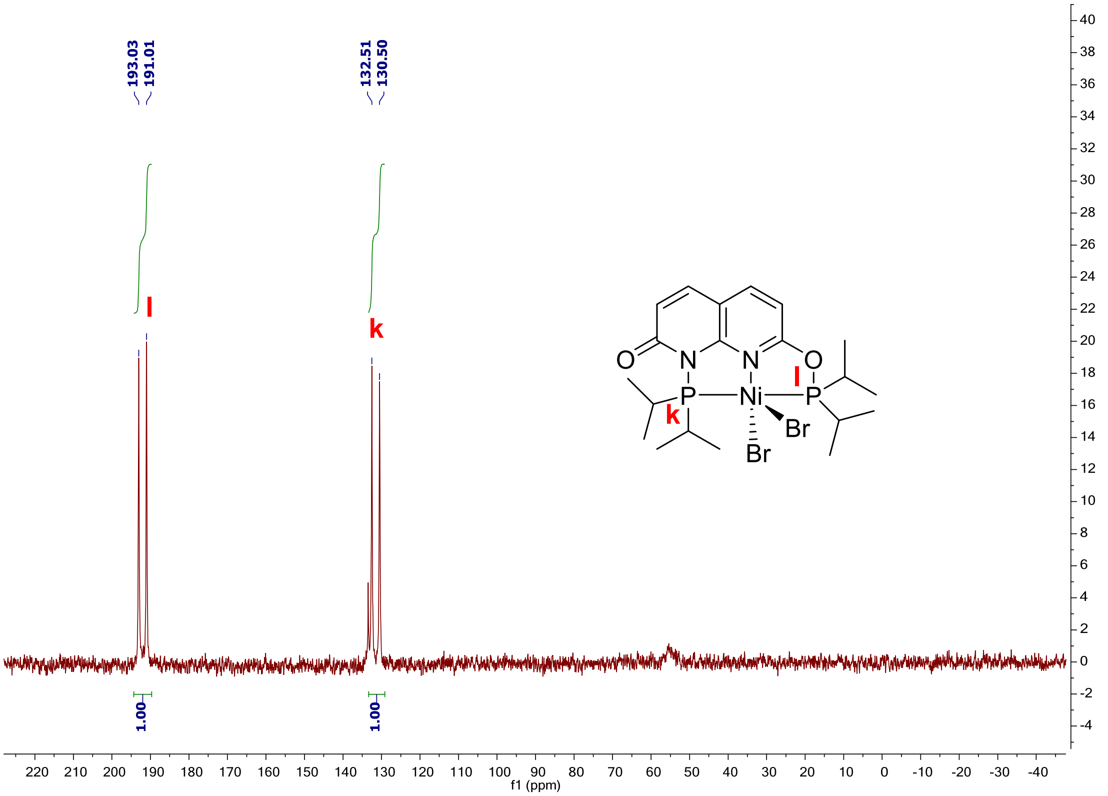

Figure S11: The ^{31}P NMR spectrum of **2** in CD_2Cl_2 at 25 °C.

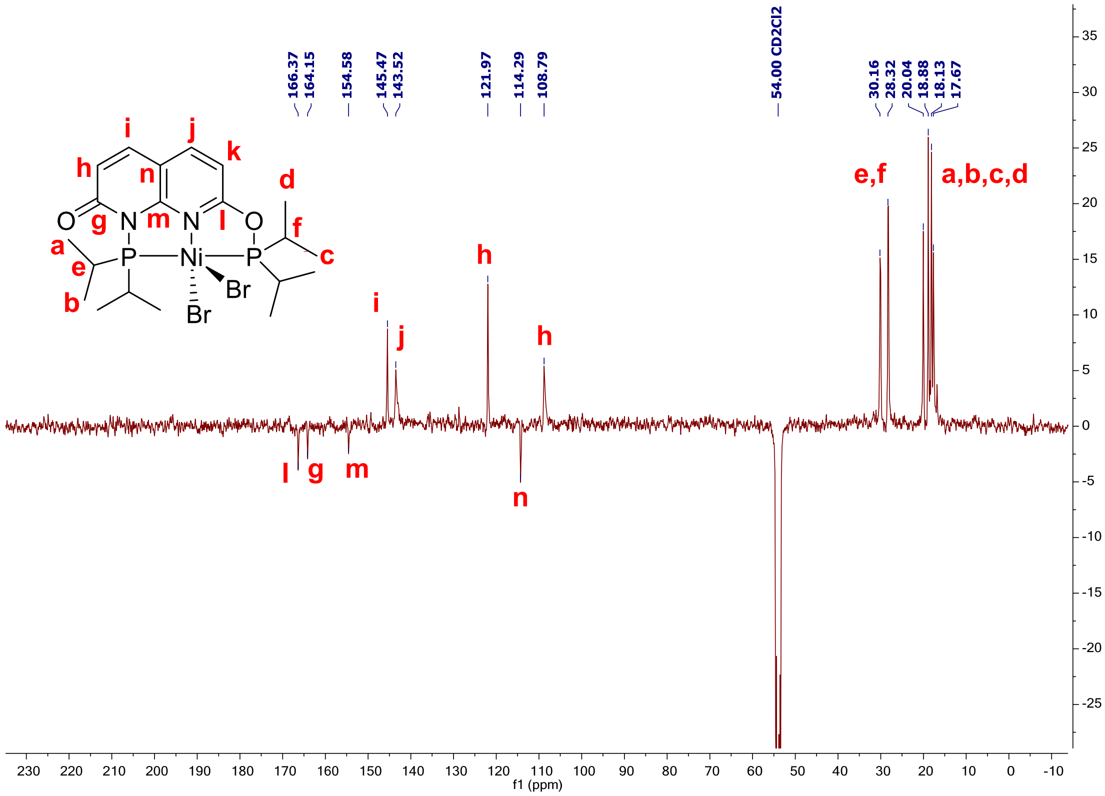

Figure S12: The ^{13}C (APT) NMR spectrum of **2** in CD_2Cl_2 at 25 °C.

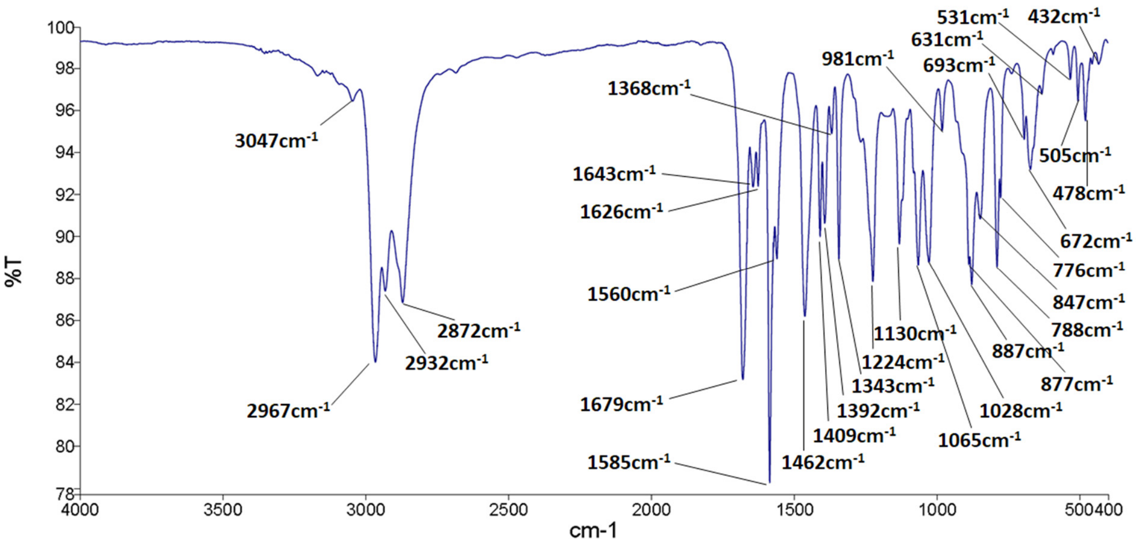

Figure S13: The IR-spectrum of **2**.

Variable temperature NMR analysis of complex 1

To assess whether the broadness of the resonance in the ^{31}P NMR spectrum of **1** was due to a fluxional process at the NMR time scale, ^{31}P and ^{1}H NMR spectra were recorded between -75 and +80 ºC. The sample of **1** in toluene-d$_8$ was prepared in a J. Young type NMR tube and was first cooled to -75 °C inside the NMR spectrometer. ^{31}P (Figure S14) and ^{1}H NMR (Figure S15-S16) spectra were recorded with regular intervals until RT. Subsequently the sample was heated to +80 ºC inside the NMR spectrometer and ^{31}P (Figure S17) and ^{1}H NMR (Figure S18-S19) spectra were recorded with regular intervals until RT. The formation of additional resonances after heating suggests the partial decomposition of complex **1** under these conditions.

The ^{1}H NMR spectra show subtle broadening of the resonances that is typically observed at lower temperatures. In contrast, the broadness of the resonance in the 31P NMR spectrum solely decreases at lower temperatures. This is the opposite of what is expected for a fluxional process on the NMR timescale but is not uncommon for broadening of the resonance due to quadrupolar relaxation arising from ^{63}Cu and ^{65}Cu (both $I = 3/2$) nuclei.[4]

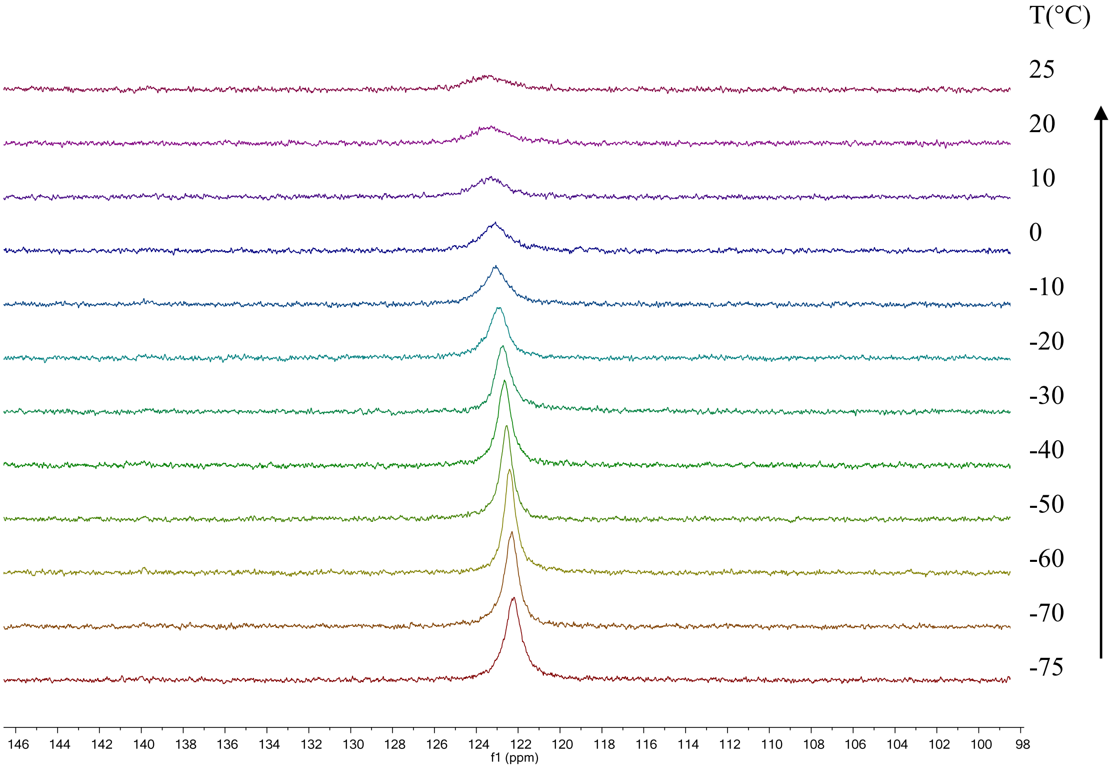

Figure S14: Stacked ^{31}P NMR spectra of **1** in toluene-d$_8$ between -75 and + 25 ºC. The arrow indicates the order in which the spectra were recorded.

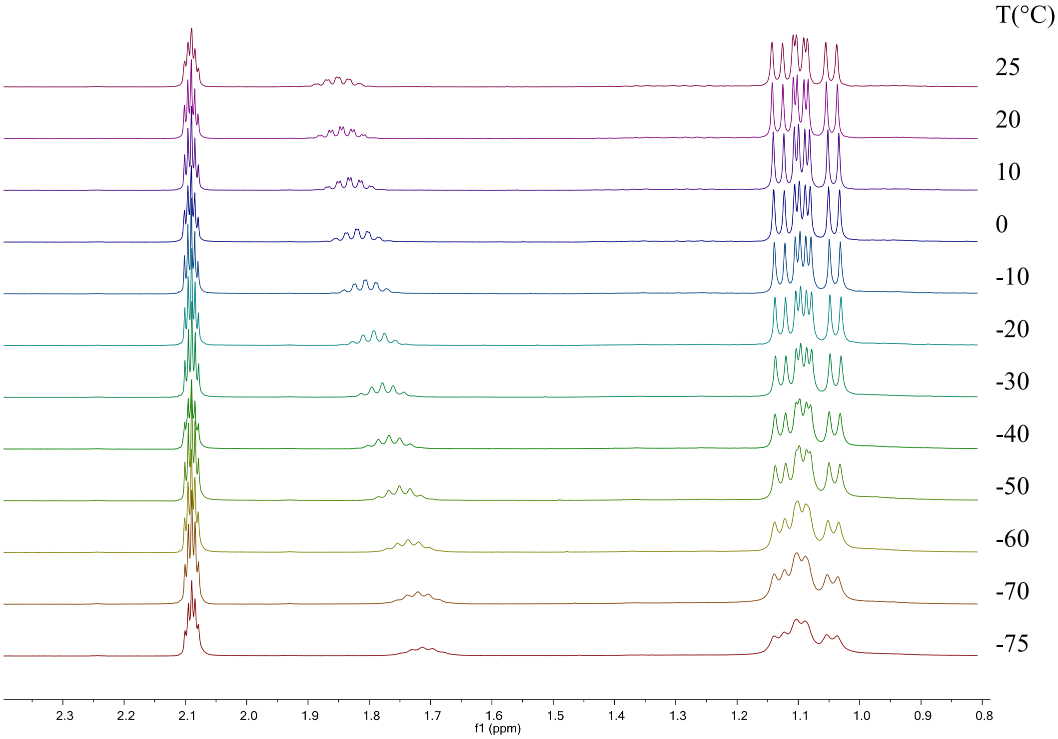

Figure S15: Stacked ^1H NMR spectra of **1** in toluene-d_8 between -75 and +25 ºC, zoomed in on the aliphatic region.

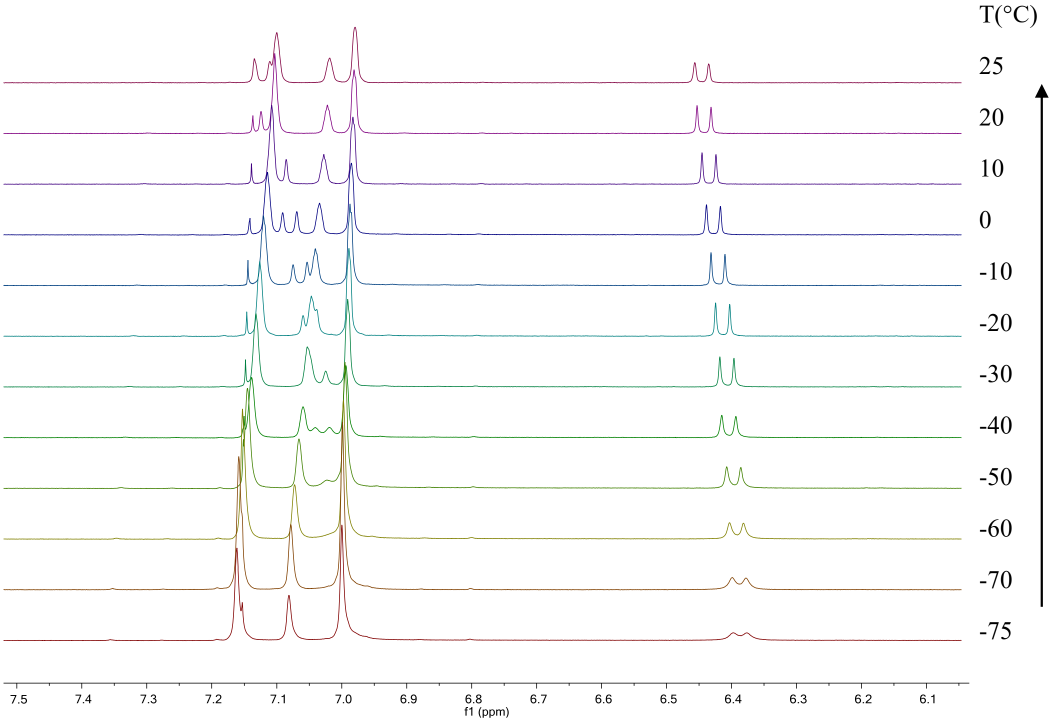

Figure S16: Stacked ^1H NMR spectra of **1** in toluene-d_8 between -75 and +25 ºC, zoomed in on the aromatic region. The arrow indicates the order in which the spectra were recorded.

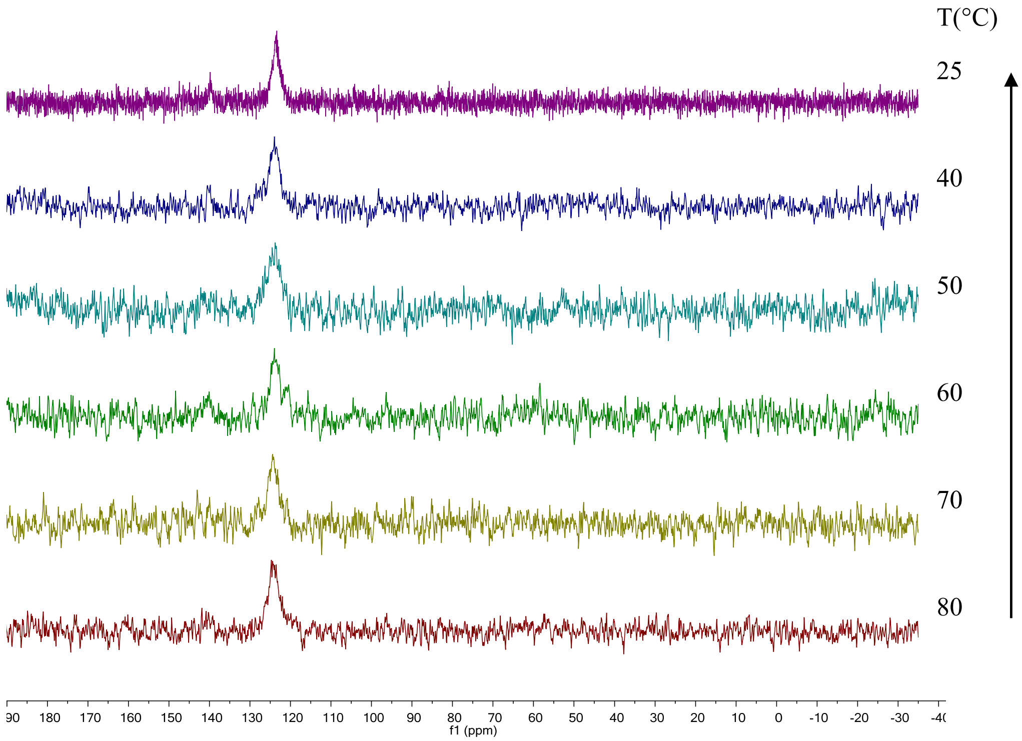

Figure S17: Stacked ^{31}P NMR spectra of **1** in C_7D_8 between +25 and +80 ºC. The arrow indicates the order in which the spectra were recorded.

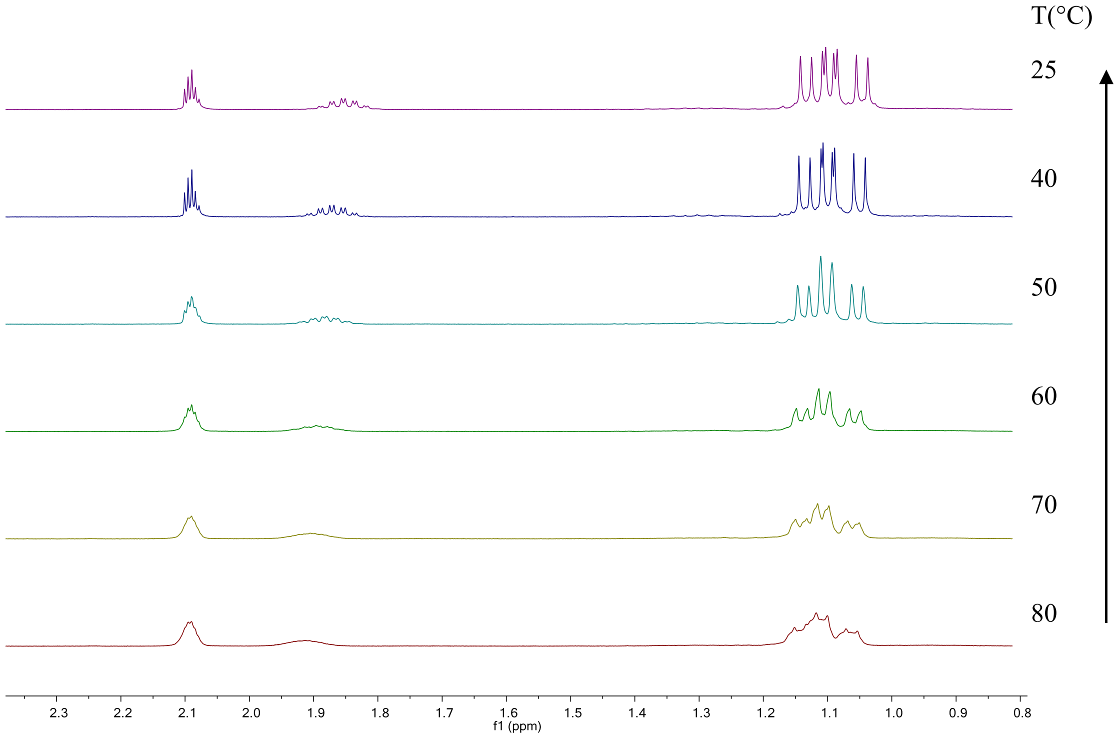

Figure S18: Stacked ^{1}H NMR spectra of **1** in toluene-d_8 between +25 and +80ºC, zoomed in on the aliphatic region. The arrow indicates the order in which the spectra were recorded.

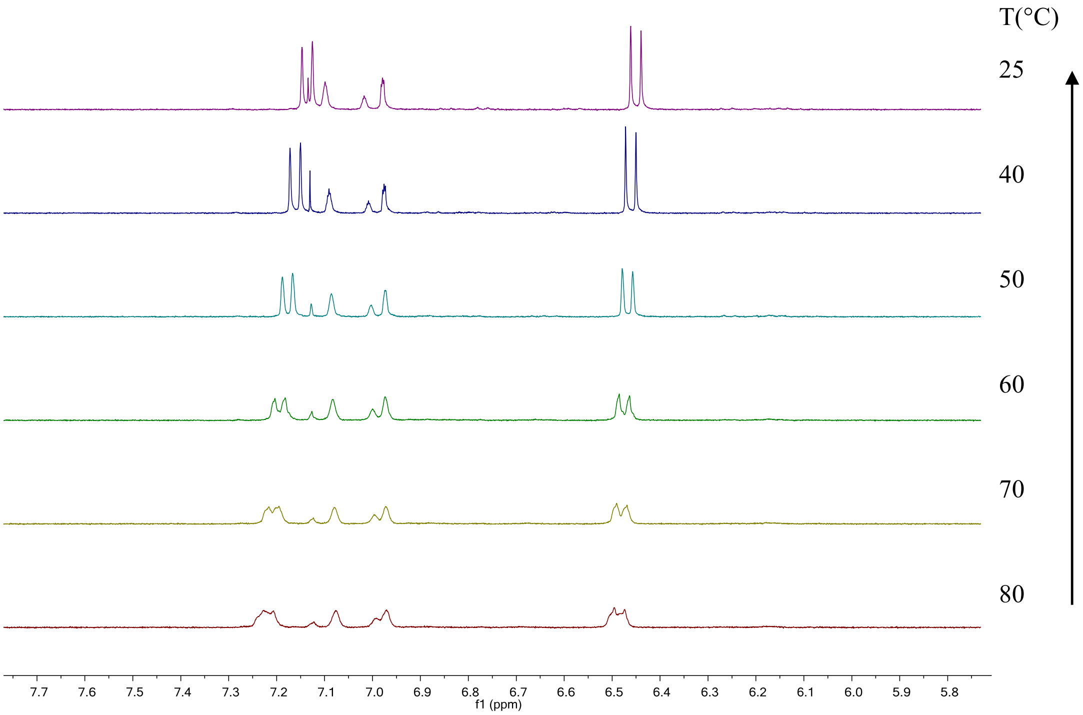

Figure S19: Stacked ^{1}H NMR spectra of **1** in toluene-d$_8$ between +25 and +80°C, zoomed in on the aromatic region. The arrow indicates the order in which the spectra were recorded.

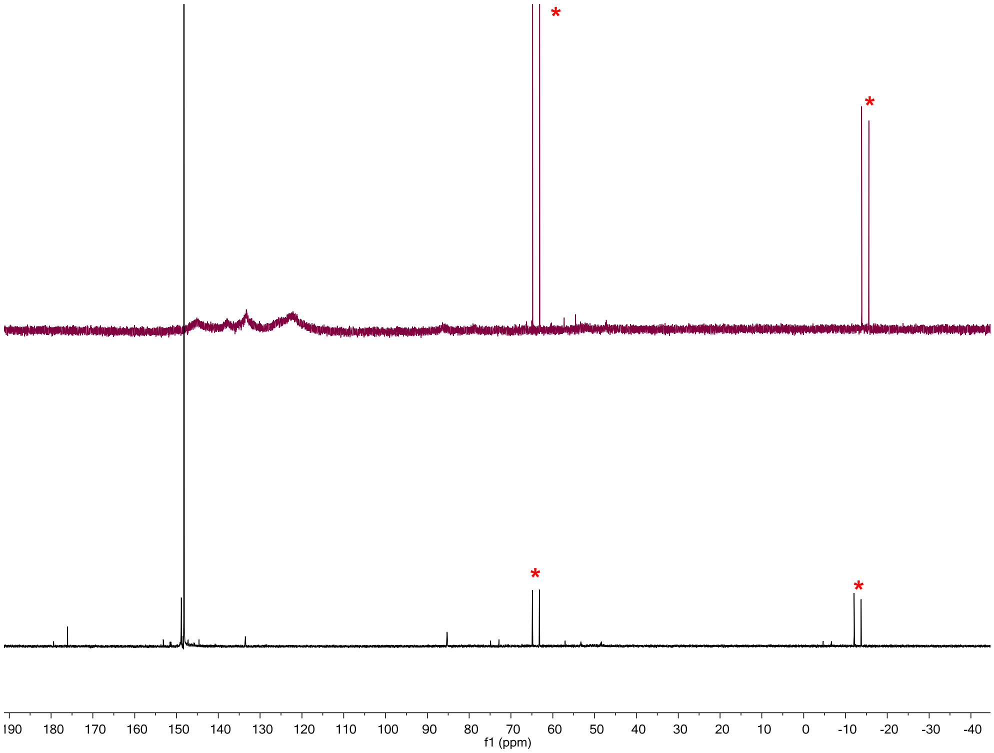

Figure S20: Stacked ^{31}P NMR spectra of the reaction mixture of the attempted *in situ* synthesis of $^{i\text{-Pr}}$PONNPCuCl (top) and ligand starting material (bottom), in MeCN at 25 °C. The broadness of the various resonances in the top spectrum prohibit observation of the trans ^2J coupling in the desired product. The resonances labelled with a * are the unidentified impurity in the ligand starting material.

Susceptibility of $^{i\text{-Pr}}$PONNOP towards hydrolysis, aminolysis and alcoholysis

The $^{i\text{-Pr}}$**PONNOP** ligand is very susceptible to hydrolysis. When the ligand is exposed to residual amounts of water in solvents, full and partial hydrolysis is observed. Full hydrolysis results in precipitation of insoluble 2,7-dihydroxy-1,8-naphthyridine and partial hydrolysis can be observed by ^{1}H NMR analysis where a nonsymmetric naphthyridine species featuring a distinct OH resonance is observed. (Figure S21). The same nonsymmetric species is also observed as an intermediate in the synthesis of $^{i\text{-Pr}}$**PONNOP** (Figure S22).

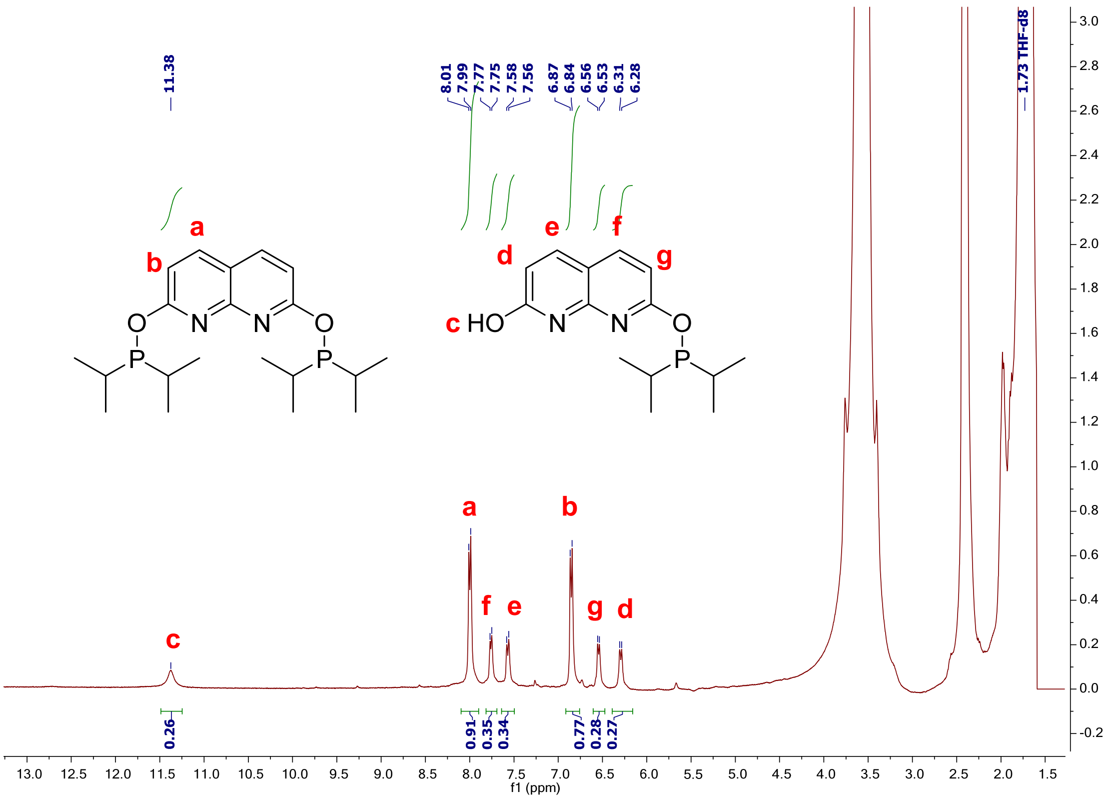

Figure S21: The ^{1}H NMR spectrum of $^{i\text{-Pr}}$**PONNOP** and the intermediate $^{i\text{-Pr}}$PONNOH in non-deuterated THF at 25 °C.

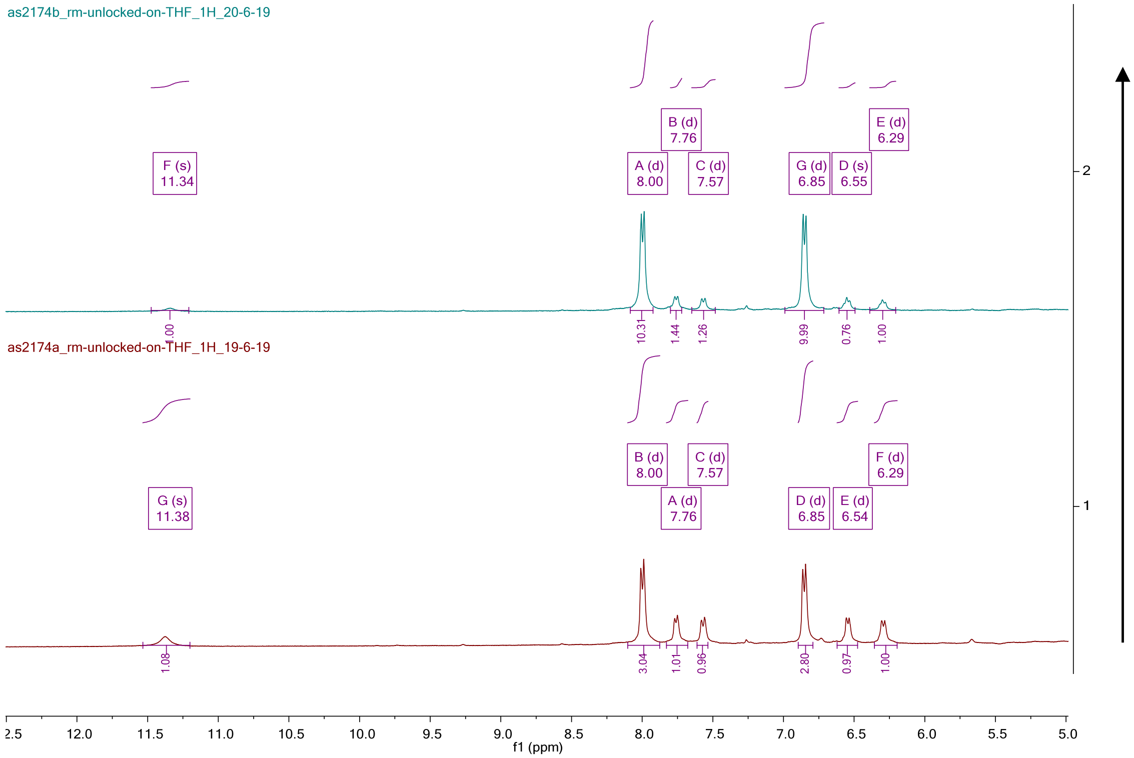

Figure S22: Stacked ^{1}H NMR spectra in THF-H_8 at 25 °C of samples taken from the reaction mixtures of the synthesis of $^{i\text{-}Pr}$**PONNOP**. The arrow indicates the order in which the spectra were taken and the top spectrum shows that concentration of $^{i\text{-}Pr}$PONNOH has diminished with respect to that of $^{i\text{-}Pr}$**PONNOP**.

$^{i\text{-Pr}}$**PONNOP** is also susceptible to aminolysis, which is showcased in the following experiment.

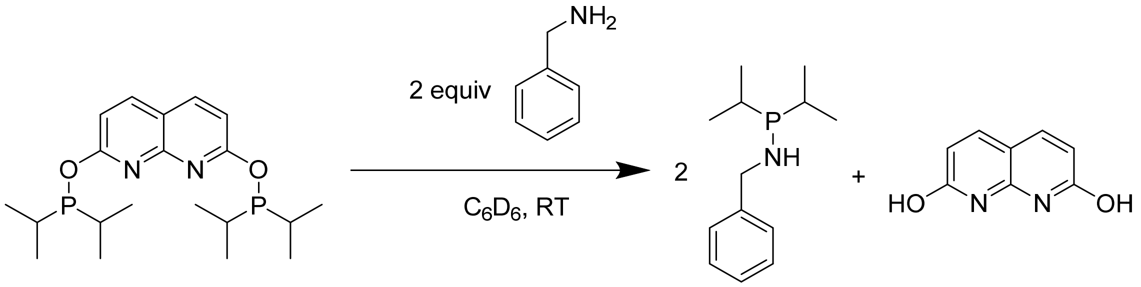

Benzylamine (19 µL, 172 µmol) was added to a solution of $^{i\text{-Pr}}$**PONNOP** (34.1 mg, 86 µmol) in C_6D_6 (0.8 mL). Within minutes, a pale yellow substance precipitates, which was characterized as 2,7-dihydroxy-1,8-naphthyridine by ^{1}H NMR analysis in DMSO-d_6. The ^{1}H and ^{31}P NMR spectra of the remaining solution (Figure S23 and S24) feature a new species that shows the expected resonances for the proposed phosphanamine product:

^{1}H NMR (400 MHz, C_6D_6, 298 K): δ = 7.25 (d, $^3J_{H,H}$ = 7.24 Hz, 2H), 7.18 (dd, $^3J_{H,H}$ = 7.3; 3.2, 2H), 7.09 (m, 1H), 4.03 (t, $^3J_{H,H}$ = 6.5 Hz, 2H), 3.57 (s, 1H), 1.44 (dtd, 2H), 0.99 (m, 12H).

^{31}P{^{1}H} NMR (162 MHz, C_6D_6, 298 K): δ = 67.1 (s).

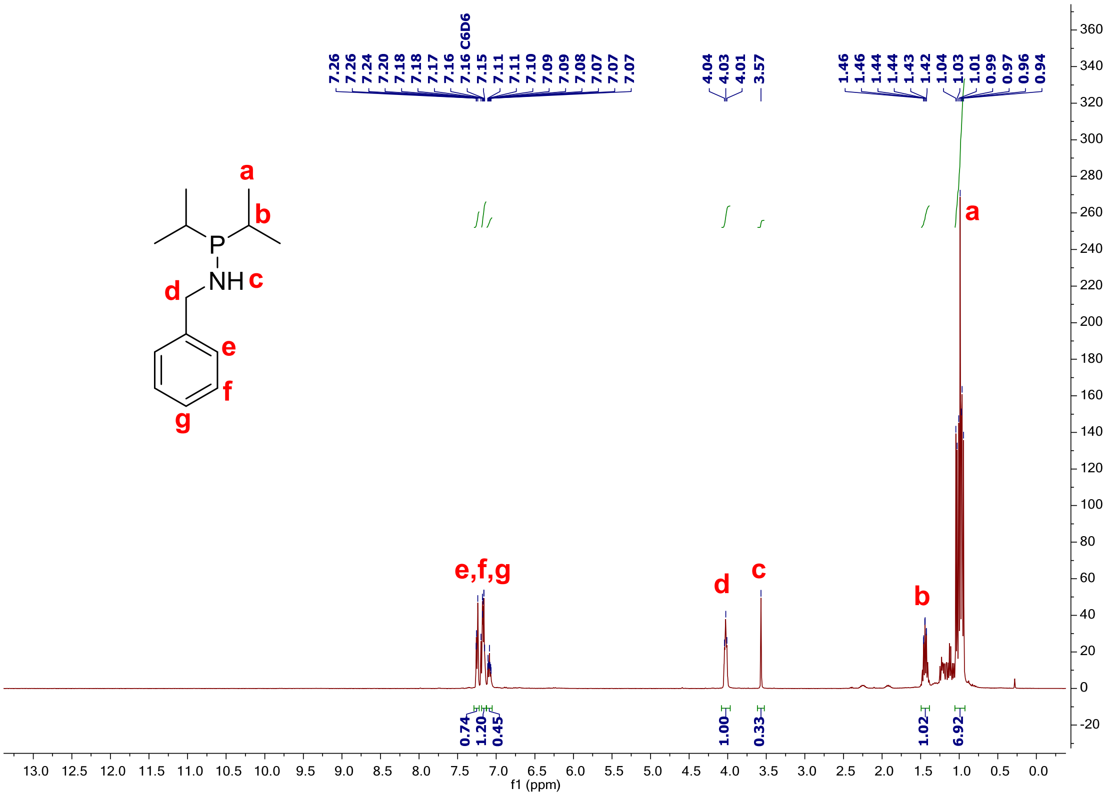

Figure S23: The ^{1}H NMR spectrum of the solution phase of a reaction of $^{i\text{-Pr}}$**PONNOP** with 2 equiv of benzylamine in C_6D_6 at 25 °C.

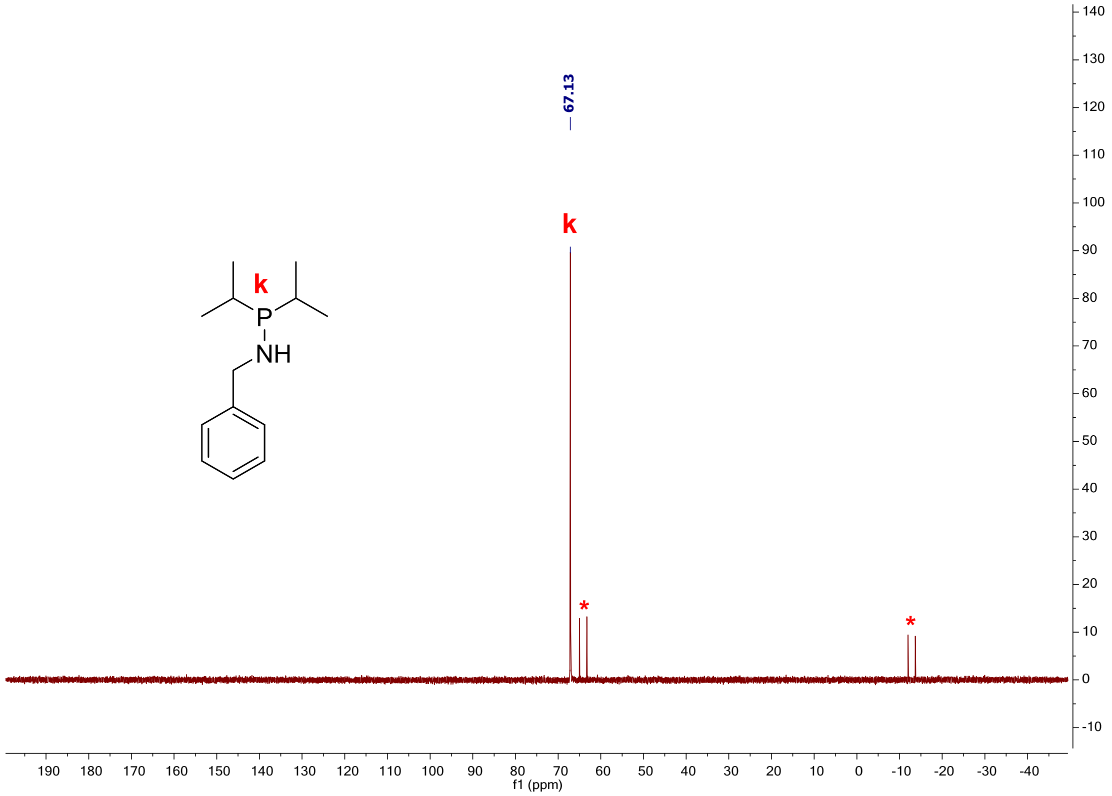

Figure S24: The ^{31}P NMR spectrum of the solution phase of a reaction of $^{i\text{-Pr}}$**PONNOP** with 2 equiv of benzylamine. in C_6D_6 at 25 °C. The resonances labelled with a * are from the unidentified impurity in the ligand starting material.

The susceptibility to alcoholysis was found serendipitously in a reaction of $^{i\text{-Pr}}$**PONNOP** with $NiCl_2$(DME) containing residual EtOH, resulting in the formation of *trans*-$NiCl_2(P(OEt)(i\text{-}Pr)_2)_2$:

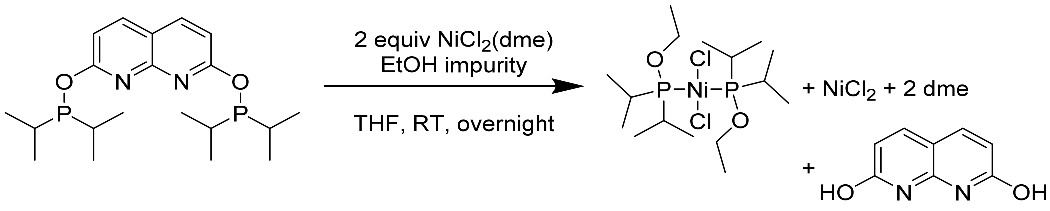

A solution of $^{i\text{-Pr}}$**PONNOP** (10.0 mg, 25 µmol) in THF (4.5 mL) was transferred to a vial containing $NiCl_2(dme)\cdot(EtOH)_x$ (11.4 mg). Instantly, a bright red suspension was formed. The mixture was stirred overnight, filtered and concentrated under a dynamic vacuum. The residue was extracted with pentane and the extracts were concentrated under a dynamic vacuum leaving a red solid (2.2 mg, 19%), which was characterized as *trans*-$NiCl_2(P(OEt)(i\text{-}Pr)_2)_2$.

^{1}H NMR (400 MHz, C_6D_6, 298 K): δ = 4.19 (q, $^3J_{H,H}$ = 6.8 Hz, 4H), 2.32 (h, $^3J_{H,H}$ = 7.1 Hz, 4H), 1.61 (d, $^3J_{H,H}$ = 7.3 Hz, 12H), 1.34 (d, $^3J_{H,H}$ = 7.1 Hz, 12H), 1.19 (t, $^3J_{H,H}$ = 6.9 Hz, 6H).

^{31}P{1H} NMR (162 MHz, CD_2Cl_2, 298 K): δ = 131.3 (s, 2P).

^{13}C{^{1}H} NMR (100 MHz, C_6D_6, 298 K): δ = 65.92 (s, 2C), 27.7 (s, 4C), 19.2 (s, 2C), 17.3 (s, 4C), 17.3 (s, 4C).

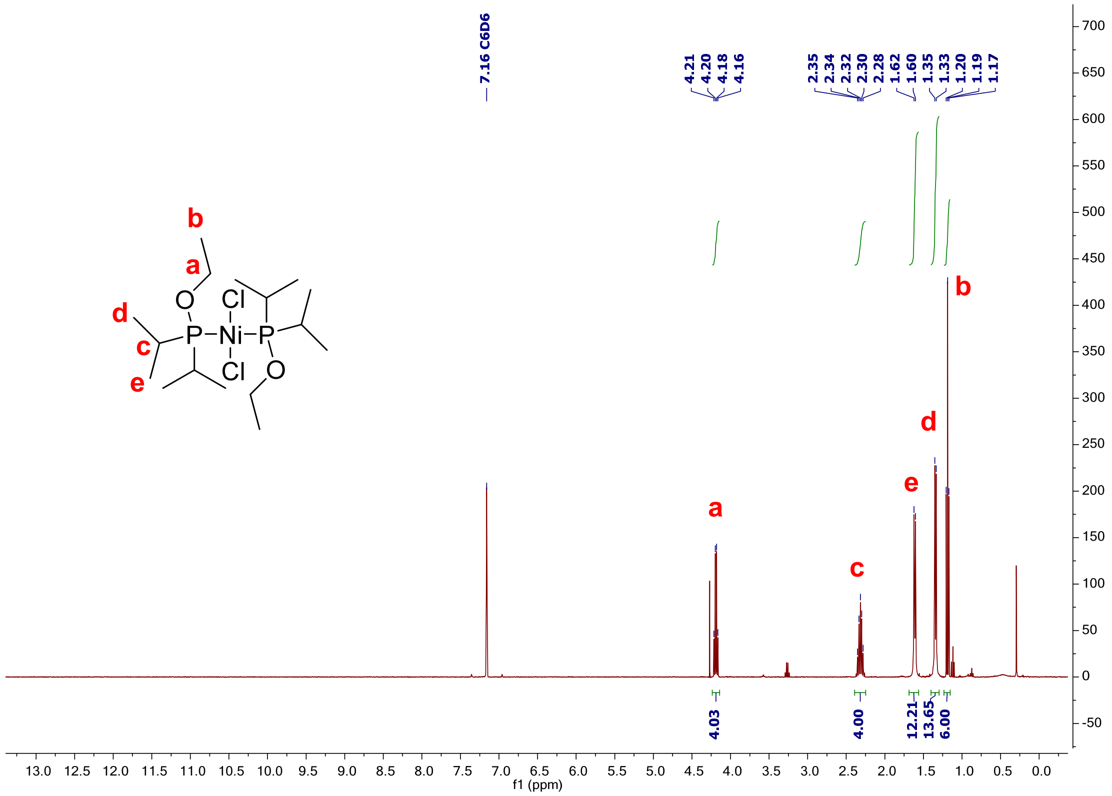

Figure S25: The ^{1}H NMR spectrum of $NiCl_2(P^{i}Pr_2(OEt))_2$ in C_6D_6 at 25 °C.

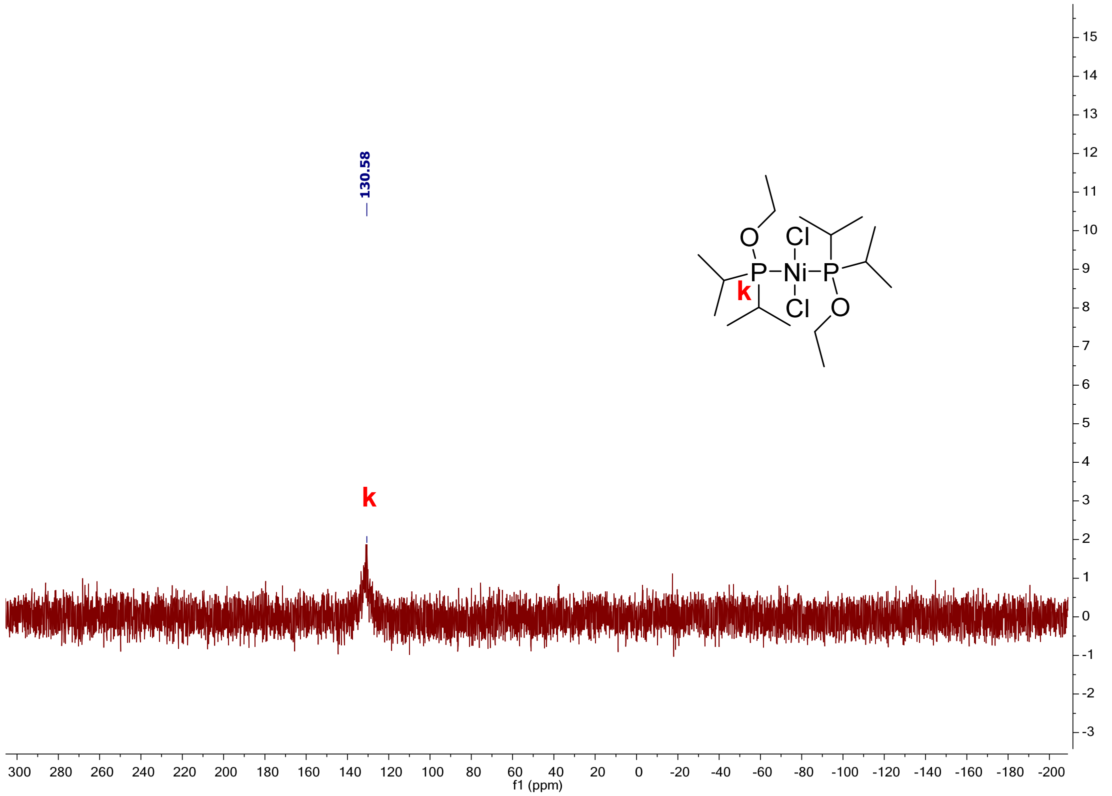

Figure S26: The ^{31}P NMR spectrum of $NiCl_2(Pi\text{-}Pr_2(OEt))_2$ in C_6D_6 at 25 °C.

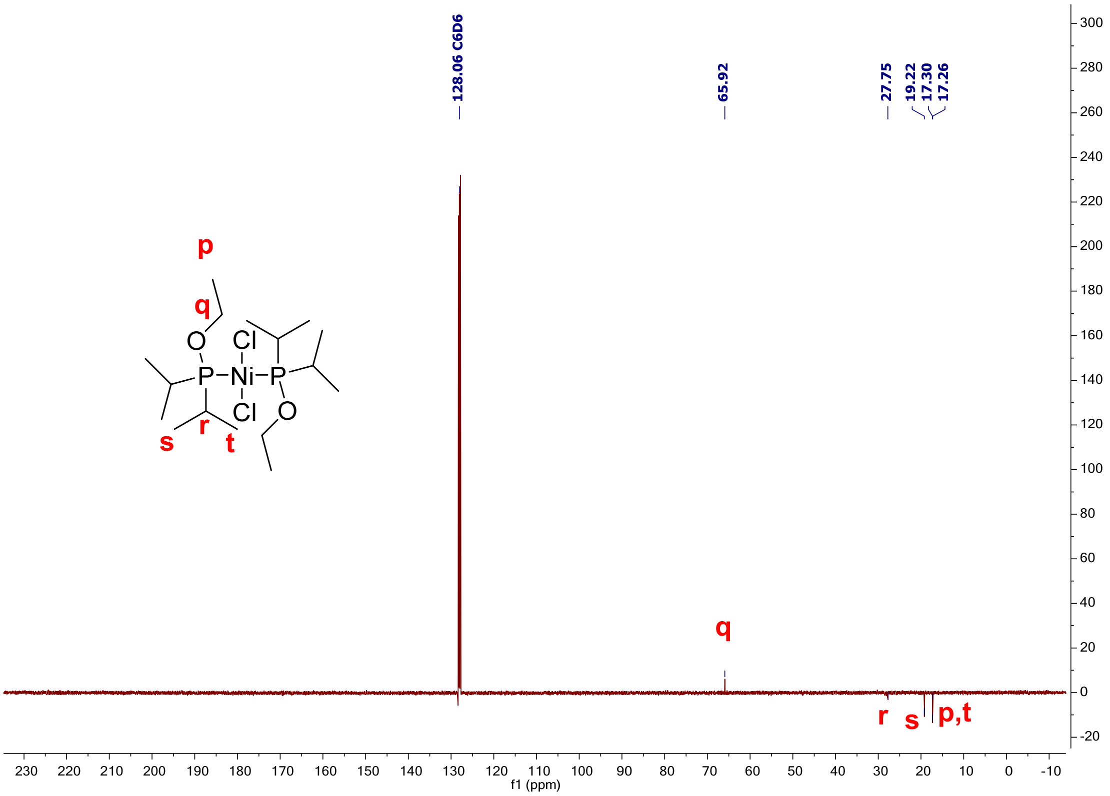

Figure S27: The ^{13}C NMR spectrum of $NiCl_2(P\textit{i}\text{-}Pr_2(OEt))_2$ in C_6D_6 at 25 °C.

Selected metric parameters of X-ray crystal structures

$NiCl_2(Pi\text{-}Pr_2(OEt))_2$ was also characterized by X-ray crystal structure determination. The solid-state structure (Figure S28) revealed a square planar mononuclear structure with exact inversion symmetry. This structure is in agreement with the obtained NMR data and is isostructural to the analogous Pd complex reported by Bedford *et al.*[5]

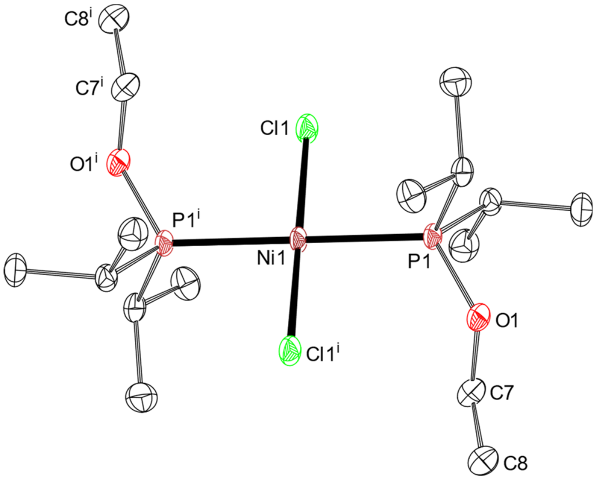

Figure S28: Displacement ellipsoid plot (50% probability) of $NiCl_2(Pi\text{-}Pr_2(OEt))_2$. Hydrogen atoms are omitted for clarity. Symmetry code *i*: -x, -y, -z.

Table S1: Selected bond lenghts in the X-ray crystal structure of *trans*-$NiCl_2(P(OEt)_2{}^iPr_2))_2$.

Bonds	**Distances (Å)**
Ni1-P1	2.2371(9)
Ni1-Cl1	2.1596(10)
P1-O1	1.624(3)
O1-C7	1.446(5)

Table S2: Selected angles in the X-ray crystal structure of *trans*-$NiCl_2(P(OEt)_2{}^iPr_2))_2$.

Angles	**Angle (°)**
Cl1-Ni1-P1	87.66(4)

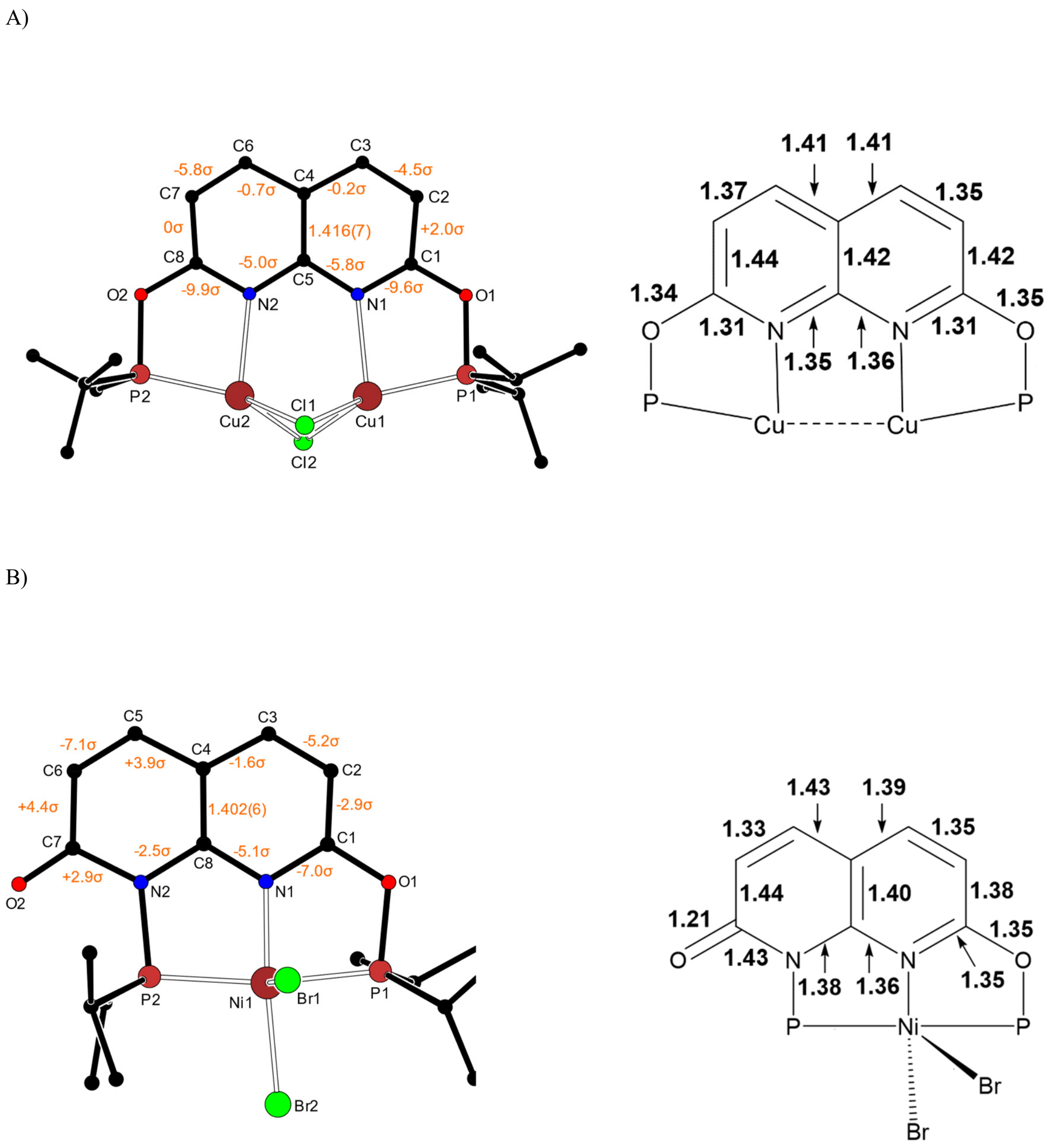

Figure S29: Left: Comparison of the distances in the ring with the central bond in the X-ray crystal structures of **1** and **2**. σ is the standard uncertainty of the difference. Note the partial dearomatization of complex **2**. Right: Schematic representations that are easily read, see table S5 and S6 for values with standard uncertainties.

Table S3: Comparison of the bond lengths in **1** with the related $^{t\text{-Bu}}$PNNPCu$_2$Cl$_2$.[6]

$^{i\text{-Pr}}$PONNOPCu$_2$Cl$_2$

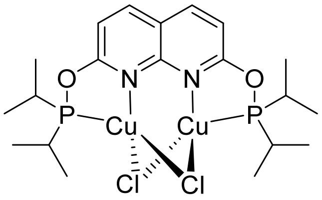

$^{t\text{-Bu}}$PNNPCu$_2$Cl$_2$

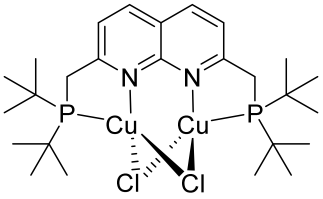

Bond	Distance (Å)	Bond	Distance (Å)
Cu1-Cu2	2.7224(9)	**Cu1-Cu1**	2.581(2)
Cu1-N1	2.185(4)	**Cu1-N1**	2.204(7)
Cu2-N2	2.183(5)		-
Cu1-P1	2.1586(19)	**Cu1-P1**	2.186(2)
Cu2-P2	2.1698(19)		-
Cu1-Cl1	2.3475(16)	**Cu1-Cl1**	2.346(3)
Cu1-Cl2	2.3282(17)		-
Cu2-Cl1	2.3482(17)		-
Cu2-Cl2	2.3582(17)		-

Table S4: Comparison of the bond angles in **1** and the related $^{t\text{-Bu}}$PNNPCu$_2$Cl$_2$.[6]

$^{i\text{-Pr}}$PONNOPCu$_2$Cl$_2$

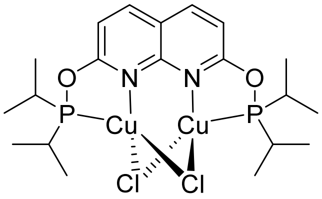

$^{t\text{-Bu}}$PNNPCu$_2$Cl$_2$

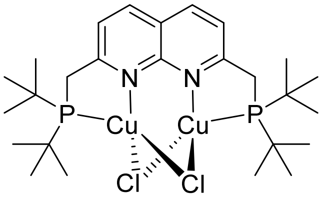

Atoms	Angle (°)	Angle (°)
Cu-Cu-N	84.16(14)	86.5(2)
	84.72(14)	-
Cu-Cu-P	167.38(6)	173.1(1)
	167.23(6)	-
P-Cu-N	83.33(14)	86.6(2)
	83.00(14)	-
Cl-Cu-Cl	95.97(6)	101.4(1)
	95.14(6)	-

Table S5: Selected Bond lengths in **1**

Bond			Distance (Å)
Cu1	-	Cl1	2.3475(16)
Cu1	-	Cl2	2.3282(17)
Cu1	-	P1	2.1586(19)
Cu1	-	N1	2.185(4)
Cu2	-	Cl1	2.3482(17)
Cu2	-	Cl2	2.3582(17)
Cu2	-	P2	2.1698(19)
Cu2	-	N2	2.183(5)
P1	-	O1	1.694(4)
P1	-	C9	1.841(7)
P1	-	C12	1.824(7)
P2	-	O2	1.690(4)
P2	-	C15	1.832(6)
P2	-	C18	1.826(7)
O1	-	C1	1.342(8)
O2	-	C8	1.350(7)
N1	-	C1	1.310(8)
N1	-	C5	1.352(8)
N2	-	C5	1.361(8)
N2	-	C8	1.307(8)
C1	-	C2	1.438(8)
C2	-	C3	1.367(9)
C3	-	C4	1.414(10)
C4	-	C5	1.416(7)
C4	-	C6	1.408(10)
C6	-	C7	1.346(10)
C7	-	C8	1.416(9)
C9	-	C10	1.523(9)

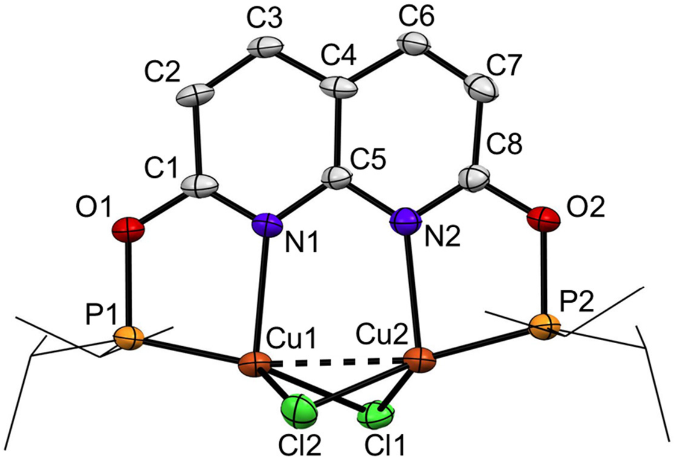

Table S6: Selected Bond lengths in **2**

Bond			Distance (Å)
Br1	-	Ni1	2.7852(8)
Br2	-	Ni1	2.3200(8)
Ni1	-	P1	2.1559(14)
Ni1	-	P2	2.1999(13)
Ni1	-	N1	1.897(4)
P1	-	O1	1.681(4)
P2	-	N2	1.770(4)
O1	-	C1	1.346(5)
O2	-	C7	1.214(6)
N1	-	C1	1.346(6)
N1	-	C8	1.361(5)
N2	-	C7	1.425(6)
N2	-	C8	1.382(6)
C1	-	C2	1.376(7)
C2	-	C3	1.355(7)
C3	-	C4	1.388(7)
C4	-	C5	1.434(7)
C4	-	C8	1.402(6)
C5	-	C6	1.338(7)
C6	-	C7	1.442(7)

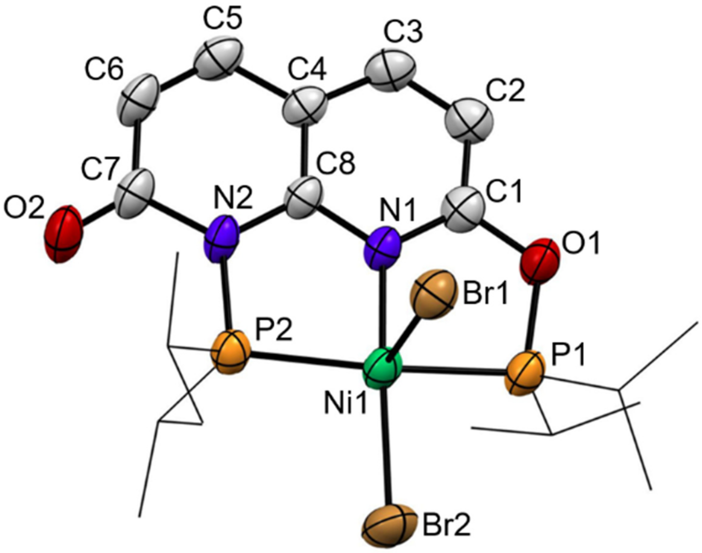

Crystallographic details

CCDC 1990856-1990858 contain the supplementary crystallographic data for this paper. These data can be obtained free of charge from The Cambridge Crystallographic Data Centre via www.ccdc.cam.ac.uk/data_request/cif.

X-ray crystal structure determination of 1

Crystals suitable for X-ray crystal structure determination were grown via slow vapour diffusion of hexane into a concentrated solution of **1** in THF.

$C_{20}H_{32}Cl_2Cu_2N_2O_2P_2 \cdot C_4H_8O$, Fw = 664.50, orange plate, 0.28 × 0.23 × 0.05 mm^3, orthorhombic, $Pna2_1$ (no. 33), a = 17.8896(5), b = 11.8315(3), c = 14.1427(4) Å, V = 2993.45(15) $Å^3$, Z = 4, D_x = 1.474 g/cm^3, μ = 1.73 mm^{-1}. The diffraction experiment was performed on a Bruker Kappa ApexII diffractometer with sealed tube and Triumph monochromator (λ = 0.71073 Å) at a temperature of 150(2) K up to a resolution of $(\sin \theta/\lambda)_{max}$ = 0.61 $Å^{-1}$. Intensity integration was performed with the Eval15 software[7]. A multi-scan absorption correction and scaling was performed with SADABS[8] (correction range 0.58-0.75). A total of 38868 reflections was measured, 5568 reflections were unique (R_{int} = 0.052), 4828 reflections were observed [$I>2\sigma(I)$]. The structure was solved with Patterson superposition methods using SHELXT[9] Structure refinement was performed with SHELXL-2018[10] on F^2 of all reflections. Inversion twinning was included in the refinement. Non-hydrogen atoms were refined freely with anisotropic displacement parameters. All hydrogen atoms were introduced in calculated positions and refined with a riding model. 325 Parameters were refined with 1 restraint (floating origin). R1/wR2 [$I > 2\sigma(I)$]: 0.0385 / 0.0871. R1/wR2 [all refl.]: 0.0500 / 0.0923. Twin fraction for inversion twinning BASF = 0.48(2). S = 1.103. Residual electron density between -0.62 and 1.02 e/$Å^3$. Geometry calculations and checking for higher symmetry was performed with the PLATON program.[11]

X-ray crystal structure determination of *trans*-$NiCl_2(P(OEt)_2{}^iPr_2))_2$

Crystals suitable for X-ray crystal structure determination were grown from a concentrated pentane solution of $NiCl_2(P^iPr_2(OEt))_2$ at -40 °C.

$C_{20}H_{32}Br_2N_2NiO_2P_2 \cdot 1.5\ C_4H_8O$, Fw = 721.10, red plate, 0.45 × 0.27 × 0.10 mm^3, triclinic, $P\overline{1}$ (no. 2), a = 8.2836(6), b = 11.8373(9), c = 16.2323(10) Å, α = 93.988(3), β = 96.686(4), γ = 93.178(3) °, V = 1573.8(2) $Å^3$, Z = 2, D_x = 1.522 g/cm^3, μ = 3.29 mm^{-1}. The diffraction experiment was performed on a Bruker Kappa ApexII diffractometer with sealed tube and Triumph monochromator (λ = 0.71073 Å) up to a resolution of $(\sin \theta/\lambda)_{max}$ = 0.65 $Å^{-1}$. Because of a phase transition during further cooling, a temperature of 250(2) K was chosen. The crystal appeared to be cracked with a rotation angle of 5.8 °

between the fragments. Consequently, two orientation matrices were used for the intensity integration with the Eval15 software[7]. A multi-scan absorption correction and scaling was performed with TWINABS[8] (correction range 0.45-0.75). A total of 43550 reflections was measured, 7265 reflections were unique (R_{int} = 0.067), 4666 reflections were observed [I>2σ(I)]. The structure was solved with Patterson superposition methods using SHELXT[9]. Structure refinement was performed with SHELXL-2018[10] on F^2 of all reflections using a HKLF5 file[12]. Non-hydrogen atoms were refined freely with anisotropic displacement parameters. One THF molecule was disordered on a general position, the other THF was disordered on an inversion center. All hydrogen atoms were introduced in calculated positions and refined with a riding model. 407 Parameters were refined with 323 restraints (distances and angles of the ^{t}butyl groups; distances, angles and displacement parameters of the disordered THF). R1/wR2 [I > 2σ(I)]: 0.0552 / 0.1392. R1/wR2 [all refl.]: 0.0994 / 0.1618. Twin fraction for two crystal fragments BASF = 0.430(3). S = 1.103. Residual electron density between -0.54 and 0.85 e/Å^3. Geometry calculations and checking for higher symmetry was performed with the PLATON program.[11]

X-ray crystal structure determination of 2

Crystals suitable for X-ray crystal structure determination were grown from a concentrated solution of **2** in a THF/hexane mixture at -40 °C.

$C_{16}H_{38}Cl_2NiO_2P_2$, Fw = 454.01, orange plate, 0.32 × 0.30 × 0.04 mm^3, triclinic, $P\overline{1}$ (no. 2), a = 7.8506(7), b = 8.2050(5), c = 9.6512(8) Å, α = 111.818(4), β = 100.304(3), γ = 97.698(3) °, V = 553.99(8) Å^3, Z = 1, D_x = 1.361 g/cm^3, μ = 1.27 mm^{-1}. The diffraction experiment was performed on a Bruker Kappa ApexII diffractometer with sealed tube and Triumph monochromator (λ = 0.71073 Å) at a temperature of 150(2) K up to a resolution of $(\sin \theta/\lambda)_{max}$ = 0.65 Å^{-1}. The crystal appeared to be cracked with a rotation angle of 4.7 ° between the fragments. Consequently, two orientation matrices were used for the intensity integration with the Eval15 software[7]. A multi-scan absorption correction and scaling was performed with TWINABS[8] (correction range 0.59-0.75). A total of 20918 reflections was measured, 2558 reflections were unique (R_{int} = 0.078), 1938 reflections were observed [I>2σ(I)]. The starting model was taken from the isostructural Pd complex.[5] Structure refinement was performed with SHELXL-2018[10] on F^2 of all reflections using a HKLF5 file[12] Non-hydrogen atoms were refined freely with anisotropic displacement parameters. All hydrogen atoms were located in difference Fourier maps and refined with a riding model. 112 Parameters were refined with no restraints. R1/wR2 [I > 2σ(I)]: 0.0536 / 0.1247. R1/wR2 [all refl.]: 0.0801 / 0.1351. Twin fraction for two crystal fragments BASF = 0.114(9). S = 1.089. Residual electron density between -0.61 and 1.34 e/Å^3. Geometry calculations and checking for higher symmetry was performed with the PLATON program.[11]

Computational Details

DFT calculations were performed with the ORCA program package, version 4.0.1.2[13] Geometries and transition states were using the BP86[14] functional using the scalar relativistically recontracted version of the Ahlrichs' triple-ζ basis set, def2-TZVP[15] on all atoms and the atom-pairwise dispersion correction with the Becke-Johnson damping scheme (D3BJ)[16]. All minima (no imaginary frequencies) and transition states (one imaginary frequency) were characterized by numerically calculating the Hessian matrix. Initial geometries for geometry optimizations were obtained from, or derived from the X-ray crystal structures. Initial geometries for transition state geometries were obtained by selecting the highest point on the crude potential energy surfaces obtained from relaxed surface scans wherein the P-O or P-N bond in the PONNOP or PONNPO minima were incrementally shortened or elongated. All input, output and .xyz files from geometry optimizations, potential energy surface scans and transition state optimizations can be downloaded for free from: http://doi.org/10.4121/uuid:8fd78884-01b0-4c37-a4ca-fb1cf4af8b61

For all three scenarios (free ligand, bound to CuCl and bound to $NiBr_2$) geometry optimizations of the minima and transition states were attempted in a singlet and triplet electronic configuration. No stable triplet configurations were found for the free ligand or for the ligand bound to CuCl. In the case of $NiBr_2$ both singlet and triplet states for all minima and transition states were found (Figure S31) but these were all higher in energy than the corresponding singlet states with one exception. The triplet state was slightly lower in energy for an additional local minimum that was found wherein the $NiBr_2$ fragment is PN bound (*PONNOP'*). This minimum is of similar energy as the PP-bound *PONNOP* $NiBr_2$. No transition state was found connecting the PN bound complex to the PP bound complex. Furthermore, a transition state search from the PN bound complex afforded the exact same TS as when we started from the PP-bound complex. Hence, these two minima likely readily interconvert, but when optimizing the geometry starting from the transition state while following the imaginary frequency the calculations afforded the PP bound complex geometry. Since we were unable to experimentally validate the computational methods, we refrain from putting much value on the relative energies of singlet and triplet states, which can be highly functional dependent. The same applies for the absolute energies between intermediates, which is why we chose to only look at the general trends.

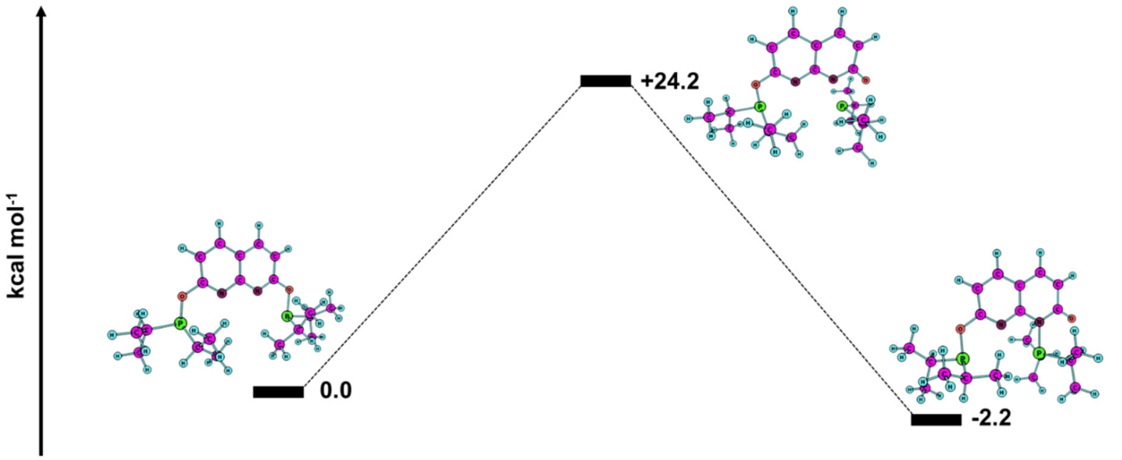

Figure S30: DFT calculated (BP86-D3, def2-TZVP) free energy profiles (ΔG^0_{298K} in kcal mol^{-1}) for the rearrangement of PONNOP to PONNP without a metal present. The black dotted line indicates the pathway to the local minima upon following the imaginary frequency in the transition state.

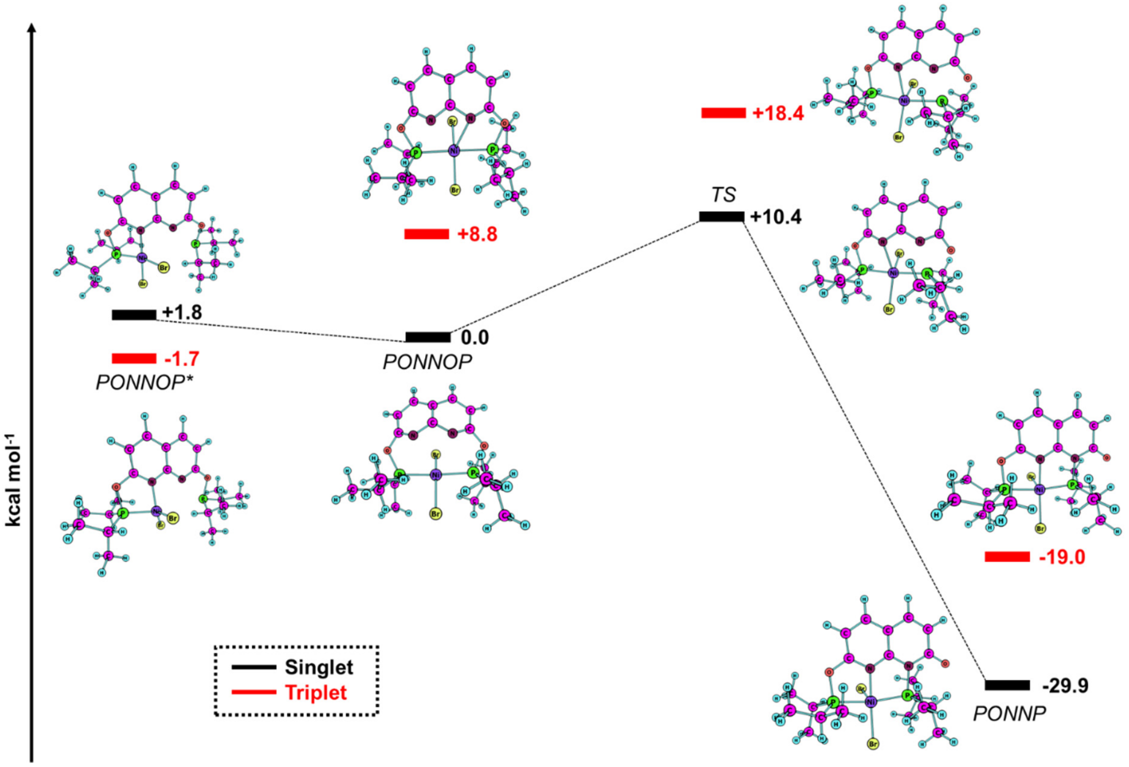

Table S31: DFT calculated (BP86-D3, def2-TZVP) free energy profiles (ΔG^0_{298K} in kcal mol^{-1}) for the rearrangement of PONNOP to PONNP when bound to NiBr$_2$. Singlet energies are depicted in black and triplet energies in red. The black dotted line indicates the pathway to the local minima upon following the imaginary frequency in the transition state (TS).

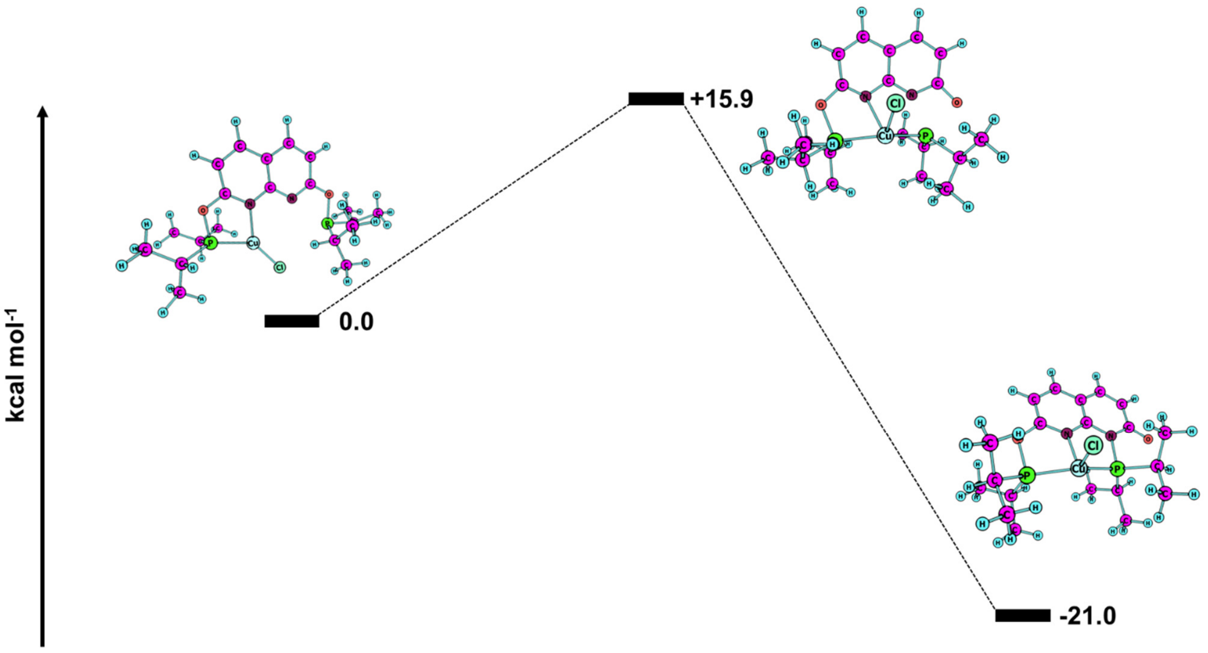

Figure S32: DFT calculated (BP86-D3, def2-TZVP) free energy profiles (ΔG^0_{298K} in kcal mol^{-1}) for the rearrangement of PONNOP to PONNP when bound to CuCl. The black dotted line indicates the pathway to the local minima upon following the imaginary frequency in the transition state.

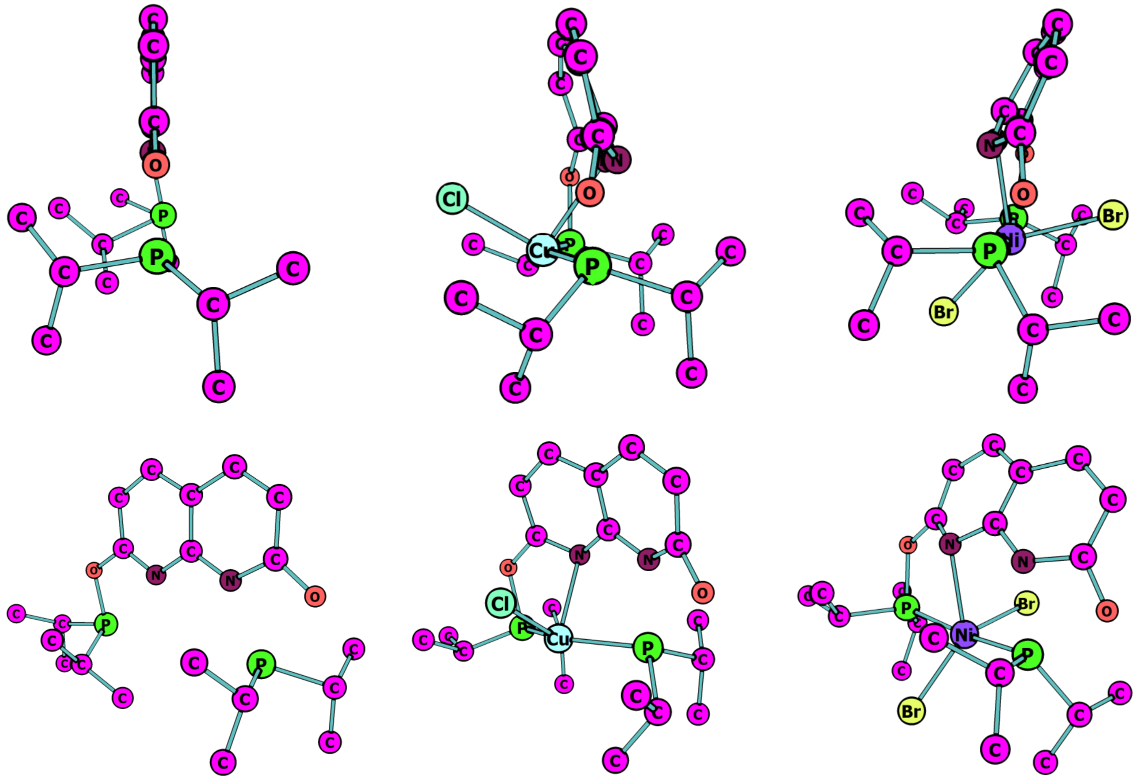

Figure S33: Side views (top) and front views (bottom) of the optimized transition state geometries that show the bending of the naphthyridine core in the presence of Cu or Ni to enable binding of the migrating P atom to the corresponding metal atom.

We hypothesize that the barrier for the conversion of PONNOP to PONNP is decreased by coordination of the migrating P atom to the transition metal, and that the barrier is lower for Ni(II) as the transition state geometries are closer to the preferred coordination geometry of Ni(II) than of that of Cu(I). As pointed out during peer-review, this hypothesis would be strengthened if similar observations were found with different metals. Hence we decided to to probe this computationally, by calculating the free energy profiles for the conversion of PONNOP to PONNP when bound to $CuBr_2$, CoCl and AgCl. For $CuBr_2$, which typically displays higher coordination numbers than Cu(I), a very similar free energy profile (Figures S34) as to what is observed for $NiBr_2$ was found featuring a relatively low reaction barrier. The coordination of P-atoms in Cu(II) complexes is rare but stable examples have been reported when the P-atoms are part of a multidentate ligand (for example Tivoto *et al.* /lnorganica Chimimica Acta **1998**, *275-276*, 401-409), which is also the case in the PONNP ligand. Ag(I) is on the other end of the scale and typically displays a low coordination number. The free energy profile for when the ligand is bound to AgCl is depicted in Figure S35 and shows that the conversion of the PONNOP to PONNP isomer is significantly less exergonic than found for all other transition metals. Similarly, the calculated reaction barrier is significantly higher. In the case of CoCl the isomerization of PONNOP to PONNP is very exergonic and the energy barrier is relatively low, but higher than what was calculated for for $CuBr_2$ and $NiBr_2$. Analysisis of the transition state geometry revealed a very early transition state wherein the migrating P atom is relatively far away from the Co atom, and this could explain why the barrier is somewhat higher. Overall, the DFT calculated free energy profiles with $CuBr_2$, CoCl and AgCl support the hypothesis that the extent of transition state stabilization is affected by the preferred coordination geometry of the transition metal. Future experimental investigations in a post COVID-19 erra should give clarity whether these computational insights hold any merit.

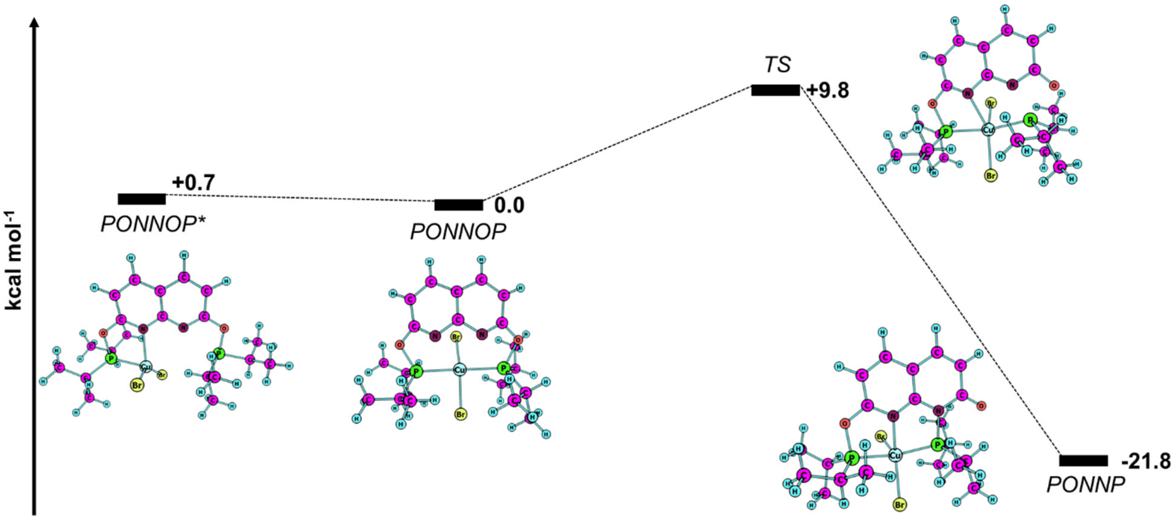

Figure S34: DFT calculated (BP86-D3, def2-TZVP) free energy profiles (ΔG^0_{298K} in kcal mol^{-1}) for the rearrangement of PONNOP to PONNP when bound to $CuBr_2$. The black dotted line indicates the pathway to the local minima upon following the imaginary frequency in the transition state.

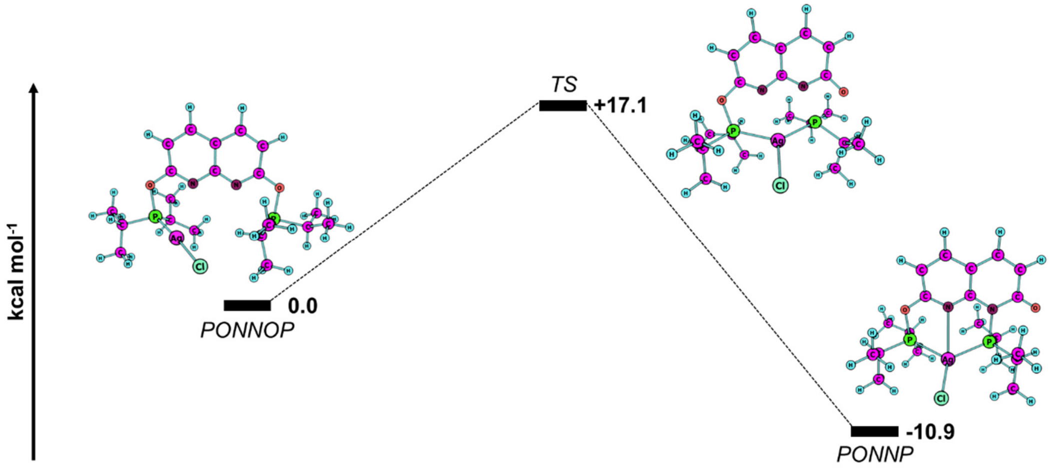

Figure S35: DFT calculated (BP86-D3, def2-TZVP) free energy profiles (ΔG^0_{298K} in kcal mol^{-1}) for the rearrangement of PONNOP to PONNP when bound to AgCl. The black dotted line indicates the pathway to the local minima upon following the imaginary frequency in the transition state.

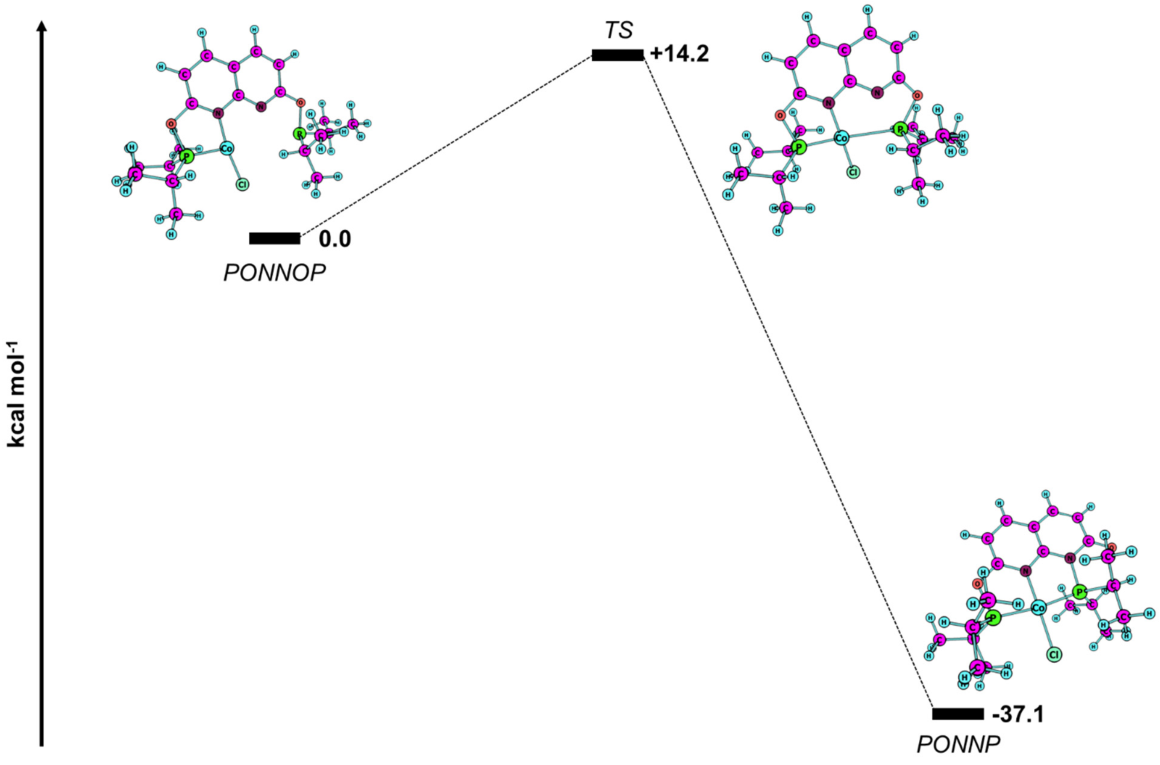

Figure S36: DFT calculated (BP86-D3, def2-TZVP) free energy profiles (ΔG^0_{298K} in kcal mol^{-1}) for the rearrangement of PONNOP to PONNP when bound to $CuBr_2$. The black dotted line indicates the pathway to the local minima upon following the imaginary frequency in the transition state.

References

---

[1] P. S. Lemport, P. N. Ostapchuk, A. A. Bobrikova, P. V. Petrovskii, N. D. Kagramanov, G. V. Bodrin and E. E. Nifant'ev *Mendeleev Commun.* **2010**, *20*, 223–225.

[2] H. Salem, L. J. W. Shimon, Y. Diskin-Posner, G. Leitus, Y. Ben-David, D. Milstein *Organometallics* **2009**, *28*, 4791-4806.

[3] W. H. Bernskoetter, S. Kloek Hanson, S. K. Buzak, Z. Davis, P. S. White, R. Swartz, K. I. Goldberg, Maurice Brookhart *J. Am. Chem. Soc.* 2009, *131*, 8603-8613.

[4] A. Marker, M. J. Gunter *J. Magn. Reson.* **1982**, *47*, 118–132.

[5] R. B. Bedford, S. L. Hazelwood, M. E. Limmert, J. M. Brown, S. Ramdeehul, A. R. Cowley, S. J. Coles, M. B. Hursthouse *Organometallics* **2003**, *22*, 1364-1371

[6] E. Kounalis, M. Lutz, D.L.J. Broere, *Chem. Eur. J.* **2019**, *25*, 13280-13284.

[7] A. M. M. Schreurs, X. Xian, L. M. J. Kroon-Batenburg. "*EVAL15*: a diffraction data integration method based on *ab initio* predicted profiles". *J. Appl. Cryst.* (2010). **43**, 70-82.

[8] G. M. Sheldrick (2014). SADABS and TWINABS. Universität Göttingen, Germany.

[9] G. M. Sheldrick. "*SHELXT* - Integrated space-group and crystal-structure determination". *Acta Cryst.* (2015). A**71**, 3-8.

[10] G. M. Sheldrick. "Crystal structure refinement with *SHELXL*". *Acta Cryst.* (2015). C**71**, 3-8.

[11] A. L. Spek. "Structure validation in chemical crystallography". *Acta Cryst.* (2009). D**65**, 148-155.

[12] R. Herbst–Irmer, G. M. Sheldrick. "Refinement of Twinned Structures with SHELXL97". *Acta Cryst.* (1998). B**54**, 443-449.

[13] F. Neese The ORCA program system. *Wiley Interdiscip. Rev. Comput. Mol. Sci.* **2012**, *2*, 73–78.

[14] (a) A. D. Becke, *J. Chem. Phys.* **1986**, *84*, 4524-4529. (b) J. P. Perdew *Phys. Rev. B* **1986**, *33*, 8822–8824.

[15] (a) D. A. Pantazis, X. -Y. Chen, C. R. Landis, F. Neese *J. Chem. Theory Comput.* **2008**, *4*, 908–919. (b) F. Weigend, R. Ahlrichs, *Phys. Chem. Chem. Phys.* **2005**, *7*, 3297–3305.

[16] (a) S. Grimme, J. Antony, S. Ehrlich, H. Krieg *J. Chem. Phys.* **2010**, *132*, 154104. (b) S. Grimme, S. Ehrlich, L. Goerigk, *J. Comput. Chem.* **2011**, *32*, 1456–1465.